

Diagnosis of an Intense Atmospheric River Impacting the Pacific Northwest: Storm Summary and Offshore Vertical Structure Observed with COSMIC Satellite Retrievals

PAUL J. NEIMAN, F. MARTIN RALPH, AND GARY A. WICK

NOAA/Earth System Research Laboratory/Physical Sciences Division, Boulder, Colorado

YING-HWA KUO, TAE-KWON WEE, AND ZAIZHONG MA

National Center for Atmospheric Research, Boulder, Colorado

GEORGE H. TAYLOR

Oregon Climate Service, Oregon State University, Corvallis, Oregon

MICHAEL D. DETTINGER

U.S. Geological Survey, Scripps Institution of Oceanography, La Jolla, California

(Manuscript received 1 February 2008, in final form 7 April 2008)

ABSTRACT

This study uses the new satellite-based Constellation Observing System for Meteorology, Ionosphere, and Climate (COSMIC) mission to retrieve tropospheric profiles of temperature and moisture over the data-sparse eastern Pacific Ocean. The COSMIC retrievals, which employ a global positioning system radio occultation technique combined with “first-guess” information from numerical weather prediction model analyses, are evaluated through the diagnosis of an intense atmospheric river (AR; i.e., a narrow plume of strong water vapor flux) that devastated the Pacific Northwest with flooding rains in early November 2006. A detailed analysis of this AR is presented first using conventional datasets and highlights the fact that ARs are critical contributors to West Coast extreme precipitation and flooding events. Then, the COSMIC evaluation is provided. Offshore composite COSMIC soundings north of, within, and south of this AR exhibited vertical structures that are meteorologically consistent with satellite imagery and global reanalysis fields of this case and with earlier composite dropsonde results from other landfalling ARs. Also, a curtain of 12 offshore COSMIC soundings through the AR yielded cross-sectional thermodynamic and moisture structures that were similarly consistent, including details comparable to earlier aircraft-based dropsonde analyses. The results show that the new COSMIC retrievals, which are global (currently yielding ~2000 soundings per day), provide high-resolution vertical-profile information beyond that found in the numerical model first-guess fields and can help monitor key lower-tropospheric mesoscale phenomena in data-sparse regions. Hence, COSMIC will likely support a wide array of applications, from physical process studies to data assimilation, numerical weather prediction, and climate research.

1. Introduction

After several days of heavy rainfall in the Pacific Northwest in early November 2006, new rainfall records were set, resulting in major flooding and damaging debris flows (e.g., Fig. 1). As with past events,

forecasters and numerical models faced the challenge of predicting this storm as it formed and evolved over the data-sparse Pacific Ocean. Partly in response to this type of challenge, a number of field studies have taken place over the eastern Pacific Ocean and along the West Coast to better understand the key phenomena involved, to document the capabilities and limitations of existing observations and models, and to improve the predictions of these damaging storms. Over the last 10 years, these have included the California Land-Falling Jets Experiment (CALJET, during 1997–98; e.g., Ralph

Corresponding author address: Paul J. Neiman, NOAA/Earth System Research Laboratory/Physical Sciences Division, Mail Code R/PSD2, 325 Broadway, Boulder, CO 80305.
E-mail: paul.j.neiman@noaa.gov

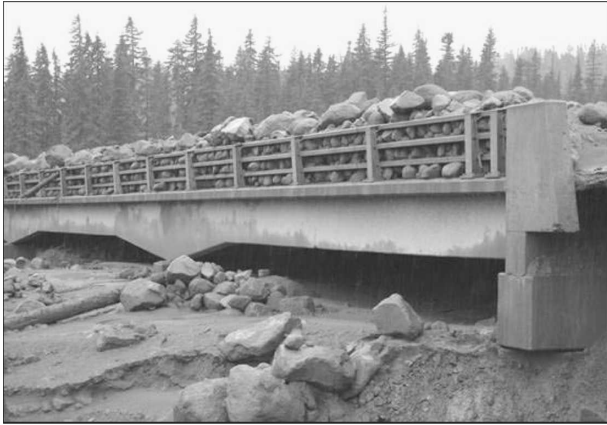


FIG. 1. The aftermath of flooding and a debris flow on the White River in OR on 7 Nov 2006. This view is of the down-river side of the White River Bridge on Highway 35, southeast of Mt. Hood. (Photo courtesy of Doug Jones, Mt. Hood National Forest.)

et al. 2003) and its follow-on counterpart the Pacific Landfalling Jets Experiment (PACJET, during 2000–01 and 2002; e.g., Neiman et al. 2005), both of which focused on the warm sector and low-level jet portion of these storms. Concurrently, the second Improvement of Microphysical Parameterization through Observational Verification Experiment (IMPROVE-2, during 2001; Stoelinga et al. 2003) focused on assessing cloud microphysics in orographic precipitation. Most recently, the Hydrometeorological Test bed (HMT, 2003 to the present; Ralph et al. 2005a) has focused on improving precipitation forecasts in these storms. Out of these field studies has emerged quantitative documentation of the key capabilities and limitations of atmospheric observations offshore and along the coast, improved understanding of the role of atmospheric rivers (ARs) in creating the type of flooding rainfall that occurred in the storm of November 2006 (Ralph et al. 2006), and the prevalence of larger precipitation amounts when landfalling storms possess AR characteristics (Neiman et al. 2008).

Atmospheric rivers are long ($>\sim 2000$ km), narrow ($<\sim 1000$ km wide) bands of enhanced water vapor flux (e.g., Zhu and Newell 1998; Ralph et al. 2004; Bao et al. 2006; Neiman et al. 2008) representing a subset corridor within a broader region of generally poleward heat transport in the warm sector of extratropical cyclones that is referred to as the “warm conveyor belt” (e.g., Browning 1990; Carlson 1991). The latent component of the poleward heat transport (i.e., the AR) can evolve differently from the sensible heat component, especially over oceanic regions where the sea surface serves as a major moisture source. Atmospheric rivers are responsible for most ($>90\%$) of the poleward water va-

por transport in less than 10% of the zonal circumference at midlatitudes (Zhu and Newell 1998; Ralph et al. 2004). Consequently, these mesoscale filamentary features play a crucial role in the global water cycle and represent a key phenomenon linking weather and climate. Most ($\sim 75\%$) of the water vapor transport within ARs occurs within the lowest 2.5 km of the atmosphere, where moist-neutral stratification is also found (Ralph et al. 2005b). The combination of lower-tropospheric moist neutrality, strong horizontal winds directed toward elevated terrain, and large water vapor content yields conditions that are ripe for the occurrence of heavy orographic precipitation (e.g., Rhea 1978; Smith 1979; Pandey et al. 1999; Rotunno and Ferretti 2001; Neiman et al. 2002) in geographically focused regions where the narrow ARs make landfall. Consequently, landfalling ARs can generate extreme precipitation, devastating floods, and debris flows along the west coasts of continents at midlatitudes (e.g., Ralph et al. 2003, 2006; Stohl et al. 2008). However, from a beneficial perspective, they also contribute significantly to the seasonal and annual rainfall and snowpack in the westernmost United States (e.g., Neiman et al. 2008) and, thus, replenish reservoirs across parts of the semiarid West.

Despite their importance to both climate and weather, ARs are poorly observed because they occur most frequently over data-sparse, midlatitude oceans. Although integrated water vapor (IWV) observations gathered from Special Sensor Microwave Imager (SSM/I; Hollinger et al. 1990) payloads aboard polar-orbiting satellites have proven crucial for monitoring these transient features over oceanic regions (e.g., Ralph et al. 2004, 2006; Neiman et al. 2008), they do not provide vertical-structure information through the ARs. Fortunately, new satellite-based global positioning system (GPS) radio occultation (RO) soundings from the Constellation Observing System for Meteorology, Ionosphere, and Climate (COSMIC) mission (e.g., Kuo et al. 1999; Rocken et al. 2000; Cheng et al. 2006) provide a new source of all-weather, open-ocean soundings of temperature and water vapor throughout the depth of the troposphere. Launched in April 2006, COSMIC currently yields ~ 2000 soundings per day distributed uniformly around the globe (Anthes et al. 2008), and it represents an advancement in RO capabilities (i.e., more uniform global coverage and greater penetration into the lower troposphere, particularly over the tropics) relative to its predecessors (e.g., Wickert et al. 2001; Tapley et al. 2004). In a revealing new study that utilizes a subset of this satellite dataset over the eastern North Pacific, Wick et al. (2008) demonstrate strong

agreement between collocated IWV retrievals from COSMIC and SSM/I. However, their study does not explore the vertical-structure characteristics of the COSMIC soundings.

The objectives of this paper are to uniquely document a high-impact AR and to explore and demonstrate the vertical profiling capabilities of the satellite-based COSMIC soundings across the otherwise data-poor eastern North Pacific Ocean. In addition to adding a new case to the growing evidence of the role of ARs in extreme precipitation events and flooding, the analysis here explores the potential of a promising new dataset during the landfall of an intense, high-impact AR in the Pacific Northwest of the United States in November 2006.

2. Observing systems

The COSMIC soundings represent the key new dataset used and assessed in this study. The COSMIC observing system consists of six satellites, each equipped with a GPS receiver. By measuring the phase delay of radio waves transmitted by GPS satellites as they are occulted by the earth's atmosphere, the COSMIC system provides vertical profiles of the radio waves' ray bending angles, under the assumption of local spherical symmetry of refractivity. From the bending angles, vertical profiles of atmospheric refractivity, which depends on pressure, temperature, and humidity, are derived and assigned to ray tangent points. Detailed descriptions of the GPS RO technique and data processing procedures can be found in Kursinski et al. (1997) and Kuo et al. (2004), respectively. It is important to note that COSMIC refractivity profiles do not provide point measurements (like a radiosonde). Rather, the inverted refractivity at a given height is represented by a horizontally weighted average with the scale that depends on the vertical gradient of the refractivity. Along a given ray path, this horizontal averaging scale ranges from ~ 250 km in the free atmosphere to ~ 100 km in the boundary layer. The scale across the ray path is ~ 1 km. The impact of the orientation of the ray paths was not considered in this study, although the favorable assessment of the COSMIC soundings in documenting the AR of November 2006 (see below) would suggest this impact is not large. The vertical resolution of the retrieved profiles is limited by diffraction effects and depends on the processing methods. Geometric optical processing applied above the troposphere results in a Fresnel vertical resolution of 0.1–1.0 km. The radio-holographic (RA-HO) processing applied in the moist troposphere utilizes the principle of synthetic aperture and yields a sub-Fresnel

resolution of several tens of meters (Gorbunov et al. 2004). In the lower troposphere, the vertical resolution is ~ 20 to 30 m.

The COSMIC soundings of temperature and water vapor in this study were generated using the COSMIC refractivity profiles in conjunction with a one-dimensional variational methodology [see online at the COSMIC Data Analysis and Archive Center (CDAAC) Web site: <http://cosmic-io.cosmic.ucar.edu/cdaac/doc/index.html>] that requires first-guess profiles such as from global analyses. Separate COSMIC sounding retrievals were generated using first-guess profiles obtained from the analyses of the National Centers for Environmental Prediction (NCEP) Global Forecast System (GFS) model at 1° resolution and the European Centre for Medium-Range Weather Forecasts (ECMWF) model at 0.5° resolution. Because both first-guess fields yield similar retrieved values of COSMIC IWV (e.g., Wick et al. 2008), the first guess from the GFS is used primarily here. Retrievals of temperature in the upper troposphere and stratosphere are relatively accurate because of very limited moisture affecting the GPS RO bending-angle measurements. In the lower troposphere, however, retrieving the temperature and water vapor pose challenges because the bending angles are affected significantly by both of these variables. Hence, the one-dimensional variational approach provides one possible solution to this ambiguity, although the cost of this method is that the retrievals are no longer independent of the numerical model fields that were used as the first guess. For the purpose of documenting ARs and other high-impact mesoscale phenomena characterized by large concentrations of low-level water vapor, the enhanced vertical resolution of COSMIC soundings in the lower troposphere (atypical of most satellite-derived sounding products) has great potential to fill a key over-ocean gap in existing observations.

The SSM/I IWV data used in this study were collected from four Defense Meteorological Satellite Program polar-orbiting satellites that have circled the globe every ~ 102 min since late 1997. The F13 and F14 satellite data were available between 1 October 1997 [start of water year (WY) 1998] and the landfalling AR in early November 2006, while the F11 and F15 satellites provided additional data from 1 October 1997 to 17 May 2000 and from 23 February 2000 to 14 September 2006, respectively. IWV data were retrieved from each SSM/I sensor in 1400-km-wide swaths over the ocean. IWV can be retrieved from the SSM/I sensor using one of several algorithms, including Schuessel and Emery (1990, hereafter SE) and Wentz (1995). Wick et al. (2008) demonstrated that the Wentz IWV compared somewhat more favorably with the COSMIC-

based IWV than did SE. However, because our paper utilizes and extends the SSM/I IWV results of Neiman et al. (2008) that were based on the SE algorithm, we have opted to use data processed with this algorithm. The use of Wentz versus SE will not adversely impact the conclusions drawn in this paper. The SSM/I sampling is synoptic and irregular in time and location. IWV retrievals are available at ~ 40 -km native resolution from each SSM/I overpass and, for this study, were composited onto a 0.25° (~ 25 km) latitude–longitude grid of the ascending and descending satellite passes for each day. For the Pacific Ocean, the ascending pass composites correspond to a time interval between 0000 and 1159 UTC, and the descending pass composites range between 1200 and 2359 UTC. These 12-h ascending and descending composites provide nearly complete spatial sampling of the domain. Multiple IWV retrievals within a grid cell were averaged, and the spatial coverage of the domain varied slightly from day to day because of the precession of the multiple orbits.

For the AR event of early November 2006, we also present ~ 10 -km resolution imagery from the *Geostationary Operational Environmental Satellite-11* (GOES-11). The $10.7\text{-}\mu\text{m}$ channel (i.e., infrared) provides surface and/or cloud-top brightness temperatures, while the $6.7\text{-}\mu\text{m}$ channel (i.e., the upper-tropospheric water vapor channel) represents the brightness temperature of a layer whose mean altitude is modulated by upper-tropospheric ($\sim 200\text{--}500$ hPa) moisture content—the greater the high-level moisture content, the higher the altitude and the lower the temperature. These satellite images were extracted from subsampled full-disk imagery.

Precipitation datasets were obtained from several networks. The National Weather Service's Cooperative Observer Program provided observations from a dense network of volunteers who report daily precipitation with storage precipitation gauges located in level, open clearings. Additional daily precipitation data were acquired from the Remote Automated Weather Stations (RAWS) array, the Snowpack Telemetry (SNOTEL) network, and the Agri-Met collection of sites. These data were then mapped onto a finescale (~ 4 km) grid using the Parameter-elevation Regression on Independent Slopes Model (PRISM; e.g., Daly et al. 1994; Hunter and Meentemeyer 2005). This climatologically based model captures the effect of variable terrain and geographic features such as coastal proximity and orographic patterns. Daily stream gauge data from U.S. Geological Survey (USGS) stream gauges along unregulated drainages were analyzed to highlight the major hydrologic impacts of the landfalling AR.

3. The landfalling atmospheric river of early November 2006

This section explores key structural and dynamical characteristics of the landfalling AR that devastated portions of the Pacific Northwest with torrential rains and severe flooding on 6–7 November 2006 (e.g., see Fig. 1). A quantitative summary analysis of the hydrological impacts of the AR is also presented. Conventional datasets (i.e., those *not* associated with COSMIC) are used in this section.

a. Standard satellite observations

Figure 2 provides a multifaceted satellite depiction of the landfalling AR during its most destructive phase on 7 November 2006. The SSM/I morning composite image (Fig. 2a) shows a well-defined narrow plume of concentrated IWV (3 to 5+ cm) extending northeastward from the tropical moisture reservoir to the Pacific Northwest, and strongly suggests direct tapping of tropical moisture into the AR.¹ The companion GOES infrared (IR) and upper-tropospheric water vapor imagery at 0600 UTC (Figs. 2b,c) show no clear indication of the AR south of $\sim 40^\circ\text{N}$, where only a curvilinear rope cloud feature was observed. This rope cloud quite likely marked the position of shallow forced ascent along the leading edge of a deep-tropospheric polar cold front (e.g., Seitter and Muench 1985; Bond and Shapiro 1991). Although ARs generally occur with polar cold fronts (e.g., Ralph et al. 2004, 2005b, 2006; Neiman et al. 2008; Stohl et al. 2008), no comparable linkage should be expected between ARs and much shallower rope clouds. The latitudinal variation of the AR in the SSM/I and IR imagery is consistent with a full-winter analysis of ARs over the eastern Pacific presented in Ralph et al. (2004). Namely, in their study, IWV contents did not change appreciably with latitude in ARs, whereas cloud-top temperatures increased significantly with decreasing latitude, to the point where a cloud-top temperature signature in the AR was no longer evident south of 30°N . This behavior quite likely reflects a general decrease in intensity of frontal circulations and an increase in intensity of Hadley subsidence with decreasing latitude.

¹ The SSM/I IWV observations alone cannot quantify moisture transport due to a lack of wind data above the surface. However, Ralph et al. (2004) established the value of using the IWV as a proxy for atmospheric river detection over the eastern Pacific during a single winter, and Neiman et al. (2008) showed a direct relationship between long, narrow IWV plumes and enhanced water vapor transport within ARs.

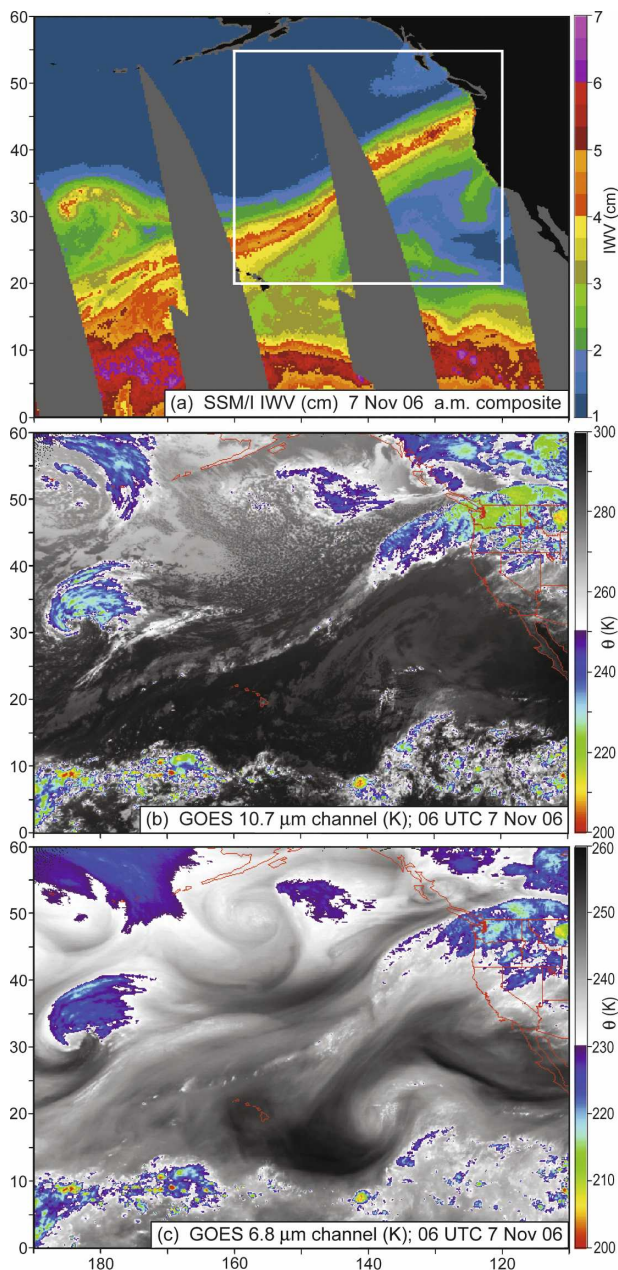


FIG. 2. Satellite imagery on the morning of 7 Nov 2006: (a) composite SSM/I image of IWV (cm) constructed from polar-orbiting swaths between \sim 0200 and 0615 UTC; (b) *GOES-11* 10.7- μ m channel (i.e., IR) image of surface and/or cloud-top brightness temperature (θ , K) at 0600 UTC; and (c) *GOES-11* 6.7- μ m channel (i.e., water vapor) image of brightness temperature (θ , K) related to the moisture content of a broad layer of the upper troposphere (approximately 200–500 hPa) at 0600 UTC. The white inset box in (a) is the domain shown in Fig. 3.

To gauge the intensity of this landfalling AR from an IWV framework, we compared its maximum IWV content within 1000 km of the coast with those ARs making landfall in western North America between 41.0° and

52.5° N during the cool season (i.e., October–March, inclusive) of the 9 water years 1998–2006.² A total of 117 AR days were catalogued in the cool season during those water years (Table 1). The methodology for creating this catalogue was first employed in Neiman et al. (2008) for water years 1998–2005. Using their approach, if a long, narrow plume of SSM/I IWV exceeded 2 cm while making landfall in the specified domain during the morning and afternoon SSM/I composites for a given day, then that day was included in the inventory. In the present study, the maximum IWV for each of those days was determined by inspecting the day's morning and afternoon composite SSM/I images for the maximum IWV encompassing ≥ 10 contiguous pixels (i.e., ≥ 6250 km²) within 1000 km of the coast. The same was done for the two AR days on 6 and 7 November 2006, thus yielding a maximum IWV value for each of the 119 AR days. The morning SSM/I composite image on 7 November (Fig. 3, inset domain in Fig. 2a) possessed a coherent 10-pixel IWV maximum of 5 cm within 1000 km of the coast (based on an IWV image color-scale resolution of 1/3 cm). Because this value was larger than that observed in the afternoon image (not shown), the maximum IWV in the landfalling AR on 7 November was 5 cm. On the previous day, the maximum IWV value was 4.67 cm.

Applying this simple methodology to all 119 AR days yields a histogram of maximum IWV (Fig. 4a). While most of the days have maximum IWV < 3.67 cm (i.e., 84%), there exists a long, skewed tail of large IWV, with the November 2006 event positioned toward the far end of the tail. In fact, the 7 November value of 5 cm is tied for second out of a total of 119 days with respect to maximum IWV. Thus, the extreme nature of the November 2006 precipitation event (described quantitatively in section 3c) is reflected in the extreme value of IWV. However, the SSM/I IWV data do not directly represent water vapor transports, even though they are closely related. Section 3c uses global reanalysis data to assess the water vapor transports in this AR, and during the 117 AR days occurring in water years 1998–2006.

b. Global reanalysis perspective

The large-scale conditions associated with the landfalling AR of early November 2006, including estimates of the horizontal water vapor transports, were gauged

² A water year is shifted 3 months earlier than a calendar year, beginning on 1 Oct and ending on 30 Sep. For example, water year 1998 starts on 1 Oct 1997 and ends on 30 Sep 1998.

TABLE 1. Dates (day, month, year) of IWV plumes with core values >2 cm intersecting the west coast of North America between 41.0° and 52.5°N during WY 1998–2006 (as in Neiman et al. 2008). Only those plumes making landfall during both the morning ascending SSM/I passes and the afternoon descending passes for a given date are included in the list.

No.	WY1998	WY1999	WY2000	WY2001	WY2002	WY2003	WY2004	WY2005	WY2006
1	1 Oct 1997	5 Oct 1998	8 Oct 1999	1 Oct 2000	10 Oct 2001	3 Oct 2002	6 Oct 2003	6 Oct 2004	10 Oct 2005
2	15 Oct 1997	6 Oct 1998	13 Oct 1999	8 Oct 2000	4 Nov 2001	27 Oct 2002	16 Oct 2003	8 Oct 2004	13 Oct 2005
3	16 Oct 1997	12 Oct 1998	17 Oct 1999	17 Oct 2000	9 Nov 2001	6 Nov 2002	17 Oct 2003	11 Oct 2004	14 Oct 2005
4	26 Oct 1997	17 Oct 1998	30 Oct 1999	22 Oct 2000	14 Nov 2001	12 Nov 2002	18 Oct 2003	12 Oct 2004	21 Oct 2005
5	29 Oct 1997	13 Nov 1998	3 Nov 1999	23 Oct 2000	15 Nov 2001	19 Nov 2002	19 Oct 2003	15 Oct 2004	22 Oct 2005
6	30 Oct 1997	14 Nov 1998	6 Nov 1999	23 Nov 2000	19 Nov 2001	12 Dec 2002	20 Oct 2003	16 Oct 2004	25 Oct 2005
7	31 Oct 1997	21 Nov 1998	11 Nov 1999		6 Jan 2002	2 Jan 2003	21 Oct 2003	22 Oct 2004	31 Oct 2005
8	2 Nov 1997	25 Nov 1998	12 Nov 1999		7 Jan 2002	26 Jan 2003	22 Oct 2003	2 Nov 2004	1 Nov 2005
9	3 Nov 1997	28 Dec 1998	13 Nov 1999		21 Feb 2002	31 Jan 2003	27 Oct 2003	5 Nov 2004	9 Nov 2005
10	5 Nov 1997	29 Dec 1998	14 Nov 1999			13 Mar 2003	29 Nov 2003	6 Nov 2004	10 Nov 2005
11	16 Dec 1997	10 Jan 1999	25 Nov 1999				22 Jan 2004	7 Nov 2004	13 Nov 2005
12	28 Dec 1997	14 Jan 1999	15 Dec 1999					8 Nov 2004	24 Dec 2005
13	23 Jan 1998	24 Feb 1999	16 Dec 1999					15 Nov 2004	30 Dec 2005
14	22 Mar 1998	27 Feb 1999						24 Nov 2004	17 Jan 2006
15								25 Nov 2004	
16								8 Dec 2004	
17								9 Dec 2004	
18								10 Dec 2004	
19								11 Dec 2004	
20								17 Dec 2004	
21								17 Jan 2005	
22								18 Jan 2005	
23								19 Jan 2005	
24								22 Jan 2005	
25								23 Jan 2005	
26								27 Mar 2005	

by constructing composite mean and anomaly³ fields using the coarse (~2.5° latitude × ~2.5° longitude) daily global gridded dataset from the National Centers for Environmental Prediction–National Center for Atmospheric Research (NCEP–NCAR) reanalysis project (Kalnay et al. 1996). The composites shown in this subsection are valid for the 2-day period on 6–7 November 2006.

Reanalysis plan-view fields of IWV and vertically integrated horizontal water vapor flux [i.e., integrated vapor transport (IVT)] for this event are presented in Fig. 5. The mean IWV analysis (Fig. 5a) shows an intense plume of moisture extending from the tropical water vapor reservoir northeastward to Washington and Oregon, as in the SSM/I imagery (Fig. 2a). The water vapor content within the core of the plume exceeded 4 cm throughout its length, also confirmed by the SSM/I imagery, although the width of this plume is

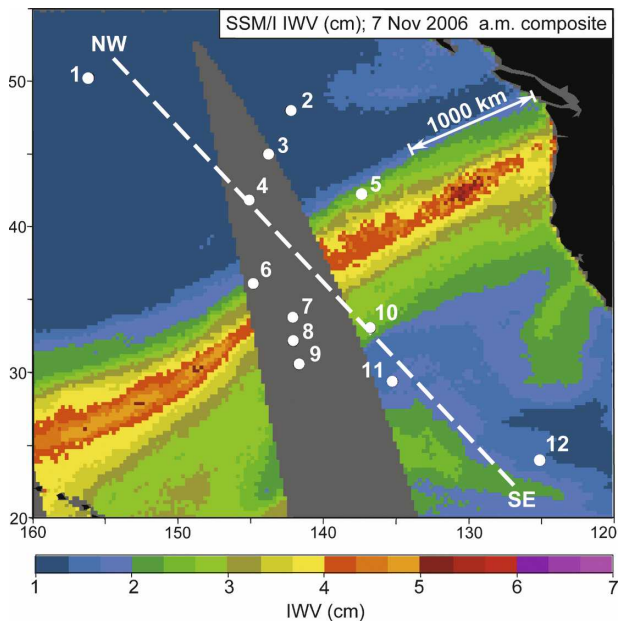


FIG. 3. As in Fig. 2a, but for a zoomed-in domain. The dashed white line NW–SE is a cross-section projection for Fig. 13. The white circles mark the locations of the 12 COSMIC soundings (listed in Table 5) used to construct this cross section.

³ Each reanalysis anomaly field presented in this paper was obtained by first calculating the relevant composite mean field for the 2-day period on 6–7 Nov 2006, and then subtracting from that mean field the long-term average for those same dates for all years in the 29-yr inclusive period between 1968 and 1996.

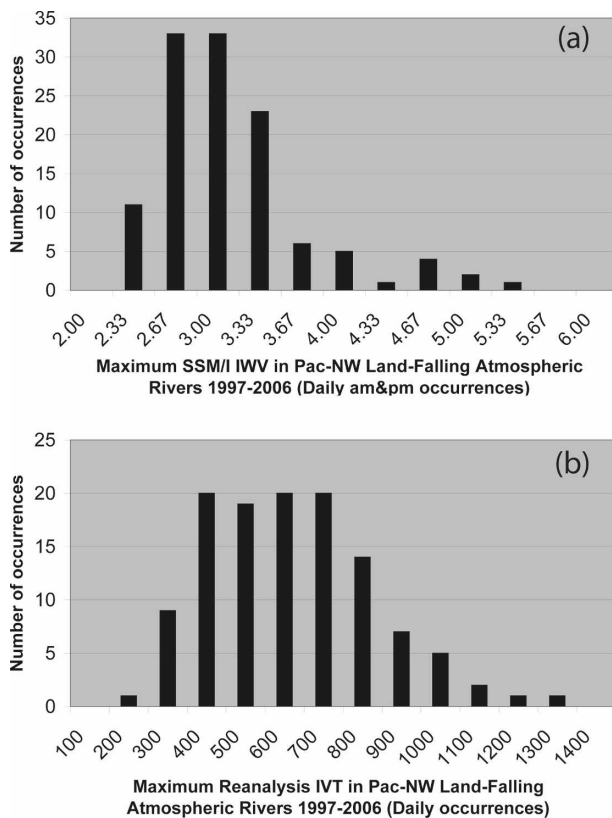


FIG. 4. (a) Distribution of the daily maximum coherent IWV content (cm) in ARs within 1000 km of the coast that made landfall in the Pacific Northwest between 41.0°N and 52.5°N latitude during water years 1998–2006. The two AR days of 6–7 November 2006 are also included. (b) Maximum daily reanalysis IVT ($\text{kg s}^{-1} \text{m}^{-1}$) within 1000 km of the coast in those ARs represented in the histogram in (a).

wider in the reanalysis due to its coarser resolution. The anomalies were quite large along the plume (Fig. 5b), attaining a maximum value of >2 cm in a ~ 2000 -km band over the eastern Pacific and terminating over western Oregon. Companion IVT analyses (Figs. 5c,d), which represent the integrated vapor transport in the troposphere between the surface and 300 hPa (see Neiman et al. 2008 for more details), underscore the exceptionally strong fluxes associated with this AR, including maximum mean and anomaly values exceeding 1000 and 800 $\text{kg s}^{-1} \text{m}^{-1}$, respectively. These large values are approximately twice as large as those reported in Neiman et al. (2008) based on an 8-yr climatology of AR landfalls in the Pacific Northwest. The orientation of these strong fluxes was nearly perpendicular to the coastal mountain ranges, thus quite likely contributing to the orographic enhancement of precipitation (e.g., Falvey and Garreaud 2007; Neiman et al. 2008; Junker et al. 2008). Both the mean and anomaly IVT fields

captured the direct tapping of tropical moisture into the AR, as the polar cold front (described in more detail below) approached low latitudes. Indeed, the poleward extrusion of water vapor from the tropics during the cool season, such as what occurred on 6–7 November 2006, is often initiated by the penetration of extratropical disturbances into the tropics (e.g., Kiladis 1998; Knippertz 2007).

In an effort to further quantify the extreme magnitude of the AR of November 2006, we determined the maximum daily reanalysis value of IVT within 1000 km of the coast in each of the 119 ARs represented in the histogram in Fig. 4a. The companion histogram of maximum IVT (Fig. 4b) shows a slightly broader peak and shorter tail than its IWV counterpart. Significantly, out of the 119 AR days, the largest daily water vapor flux ($>1300 \text{ kg s}^{-1} \text{m}^{-1}$) occurred on 6 November 2006. On the following day, the maximum IVT resided in the $1000 \text{ kg s}^{-1} \text{m}^{-1}$ bin. This high-end ranking of IVT on 6–7 November further highlights the extreme character of this landfalling AR.

Additional reanalysis fields (Fig. 6) further highlight the synoptic conditions associated with the AR on 6–7 November 2006. The mean 500-hPa geopotential height analysis (Fig. 6a) portrays a trough over the Gulf of Alaska and southwesterly flow across the eastern Pacific Ocean and Pacific Northwest. The corresponding anomaly field (Fig. 6b) shows a prominent trough-ridge couplet southeast of the Aleutians and over the western United States. At low levels, the mean 925-hPa temperature field (Fig. 6c) highlights the presence of cold-frontal baroclinicity extending northeastward from north of Hawaii to the Pacific Northwest. An intense temperature anomaly couplet straddled the front (Fig. 6d), with negative anomalies as large as -5°C south of the Aleutians and even larger positive anomalies of 7° – 12°C across the northern tier of states. Companion analyses of equivalent potential temperature (θ_e) show a narrow plume of high- θ_e air paralleling the leading edge of the cold front (Fig. 6e) in a region of very large positive θ_e anomalies (Fig. 6f). These anomalies were maximized (i.e., >20 K) across the Pacific Northwest.

The final pair of reanalysis fields (Figs. 6g,h) depict the altitude (in hPa) of the 0°C level, which serves as a first-order proxy of the precipitation melting level.⁴ The cold-frontal transition over the eastern Pacific is clearly evident in these two fields. In addition, the melting-level pressure across the Pacific Northwest (i.e., 625–700 hPa, or >3 km MSL) was ~ 135 – 150 hPa less than

⁴ The melting level typically resides 200–400 m below the 0°C isotherm (e.g., Stewart et al. 1984; White et al. 2002).

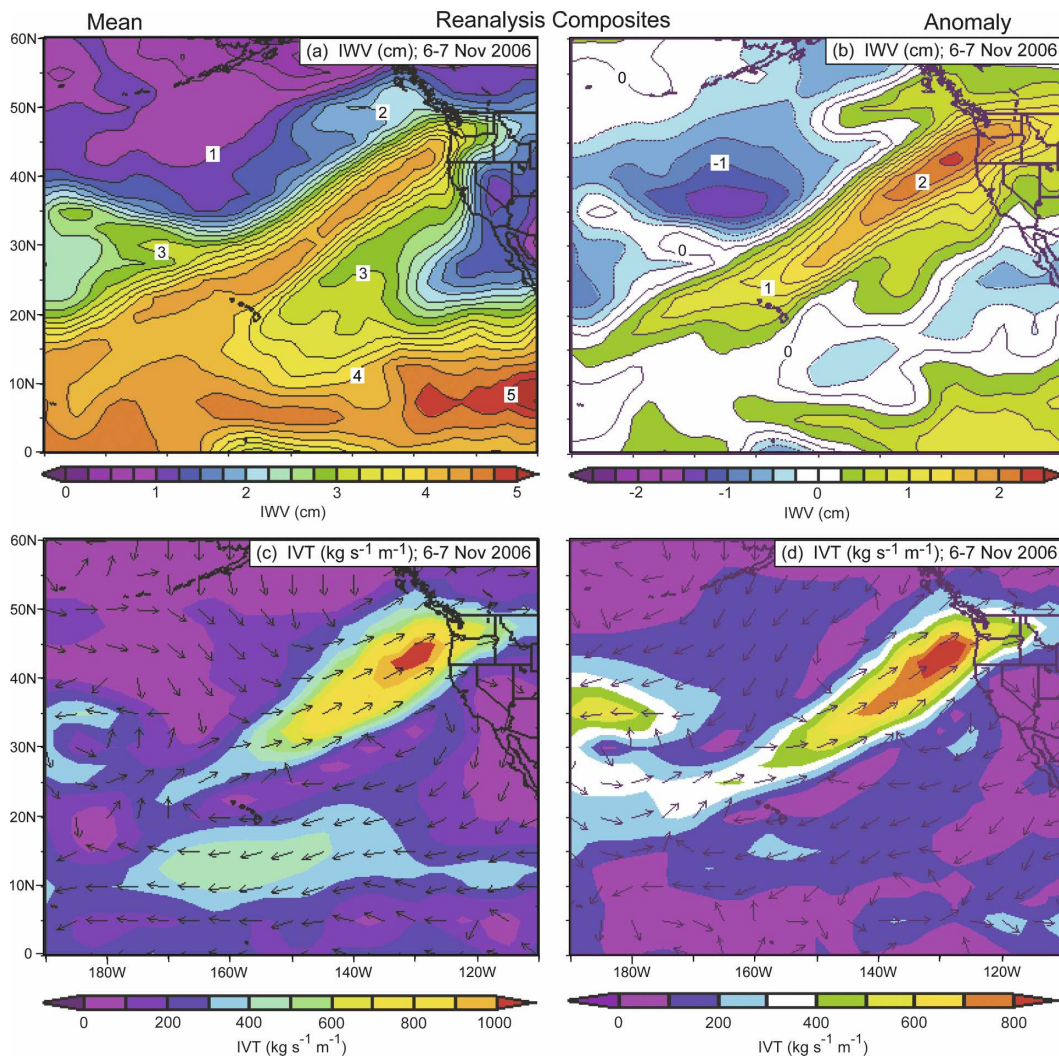


FIG. 5. Composite analyses derived from the NCEP–NCAR daily reanalysis dataset for 6–7 Nov 2006: (a), (b) IWV (cm) mean and anomaly, respectively; and (c), (d) IVT ($\text{kg s}^{-1} \text{m}^{-1}$) mean and anomaly, respectively. The vectors in (c) and (d) show the direction of IVT.

the climatological mean, which corresponds to a positive height anomaly of ~ 1200 m. These remarkably high melting levels have major hydrological implications. Most importantly, a warm storm with high melting levels will result in rain falling at high elevations over a much larger catchment area for runoff than during a typical storm. The greatly enhanced runoff volume often leads to major flooding (e.g., White et al. 2002; Lundquist et al. 2008). The contribution of snowmelt to runoff during a warm storm with high melting levels is a secondary factor leading to flooding (e.g., McCabe et al. 2007).

c. Surface-based hydrometeorological analysis

The storm of early November 2006 strongly impacted the northwestern corner of the United States, as evi-

dent in the daily surface meteorological and streamflow observations from the period (summarized in Fig. 7). Figures 7a,b show the maximum 3- and 1-day precipitation totals during the 5-day window between 5 and 9 November, regardless of when in that window they occurred. The maximum daily rainfall totals occurred on either 6 or 7 November throughout the affected area. Figure 7c shows the same 1-day totals in a climatological context, as percentages of the 100-yr daily precipitation event estimated at the observing sites. Values greater than 100% correspond to daily precipitation totals that exceeded the 100-yr daily precipitation event (i.e., that exceeded a daily event that has a 1% chance of occurring in any given year). Finally, Fig. 7d shows the ranks of the highest daily flow at each stream gauge during the 5–9 November period among all November

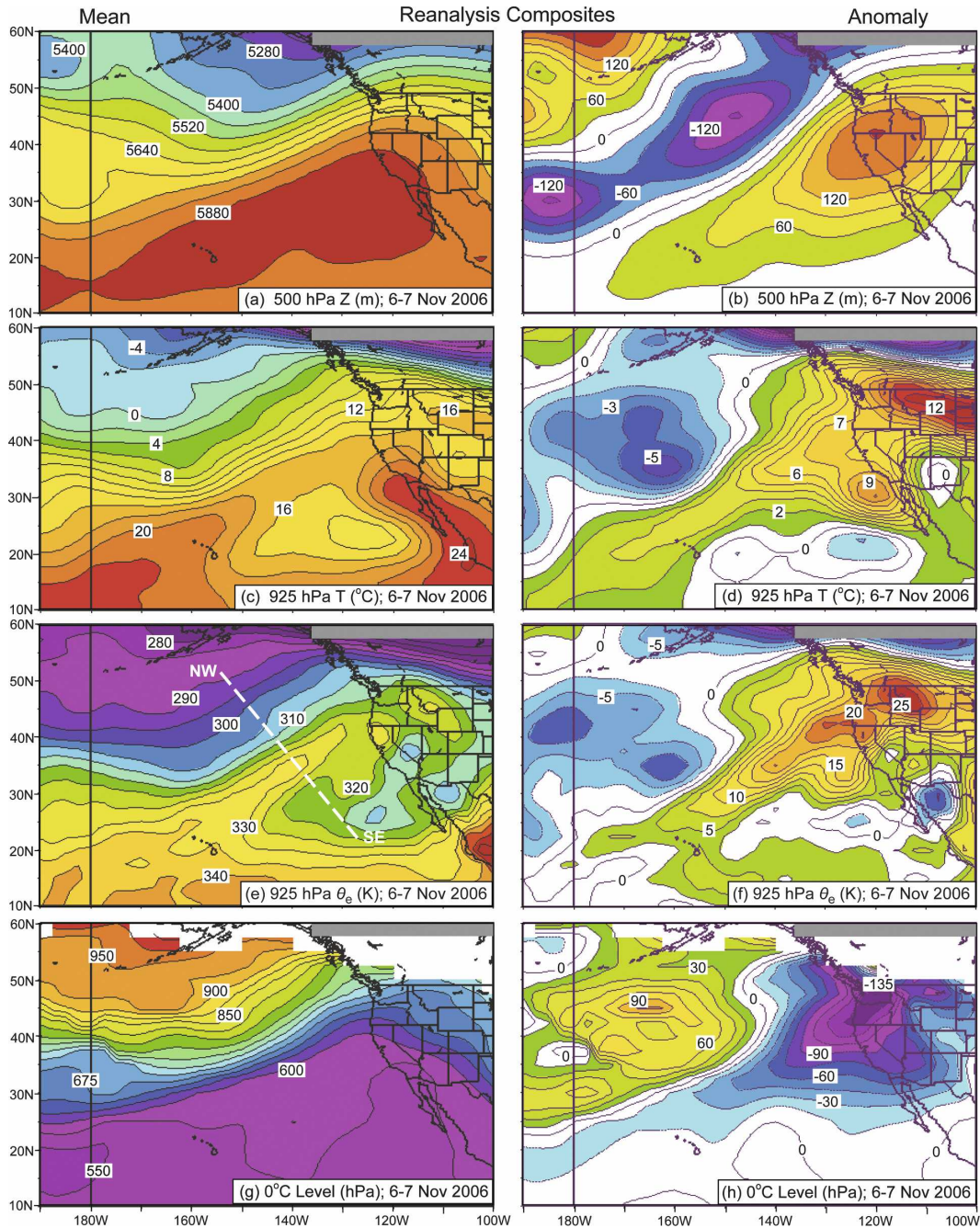


FIG. 6. As in Fig. 5, but for (a), (b) 500-hPa geopotential height (Z , m); (c), (d) 925-hPa temperature (T , $^{\circ}\text{C}$); (e), (f) 925-hPa equivalent potential temperature (θ_e , K); and (g), (h) 0°C level (hPa). The dashed white line NW-SE in (e) is the same as in Fig. 3.

days (for at least 30 yr) when flow has been recorded at that site.

Among the 3-day precipitation totals (Fig. 7a), the heaviest rain fell along the crests of the Cascades and Coastal Mountains (200–500 mm), with lesser amounts occurring in the inland ranges (50–200 mm). A small pocket of extreme 3-day rainfall exceeding 700 mm in-

undated a portion of the coast range south of the Columbia River outlet, while another small maximum in excess of 600 mm affected the Cascades north of the Columbia. The decrease in precipitation from the Cascades to the inland ranges mirrors the results in Neiman et al. (2008) based on eight winters of AR landfalls. This behavior can be attributed in large part to the

5-9 November 2006

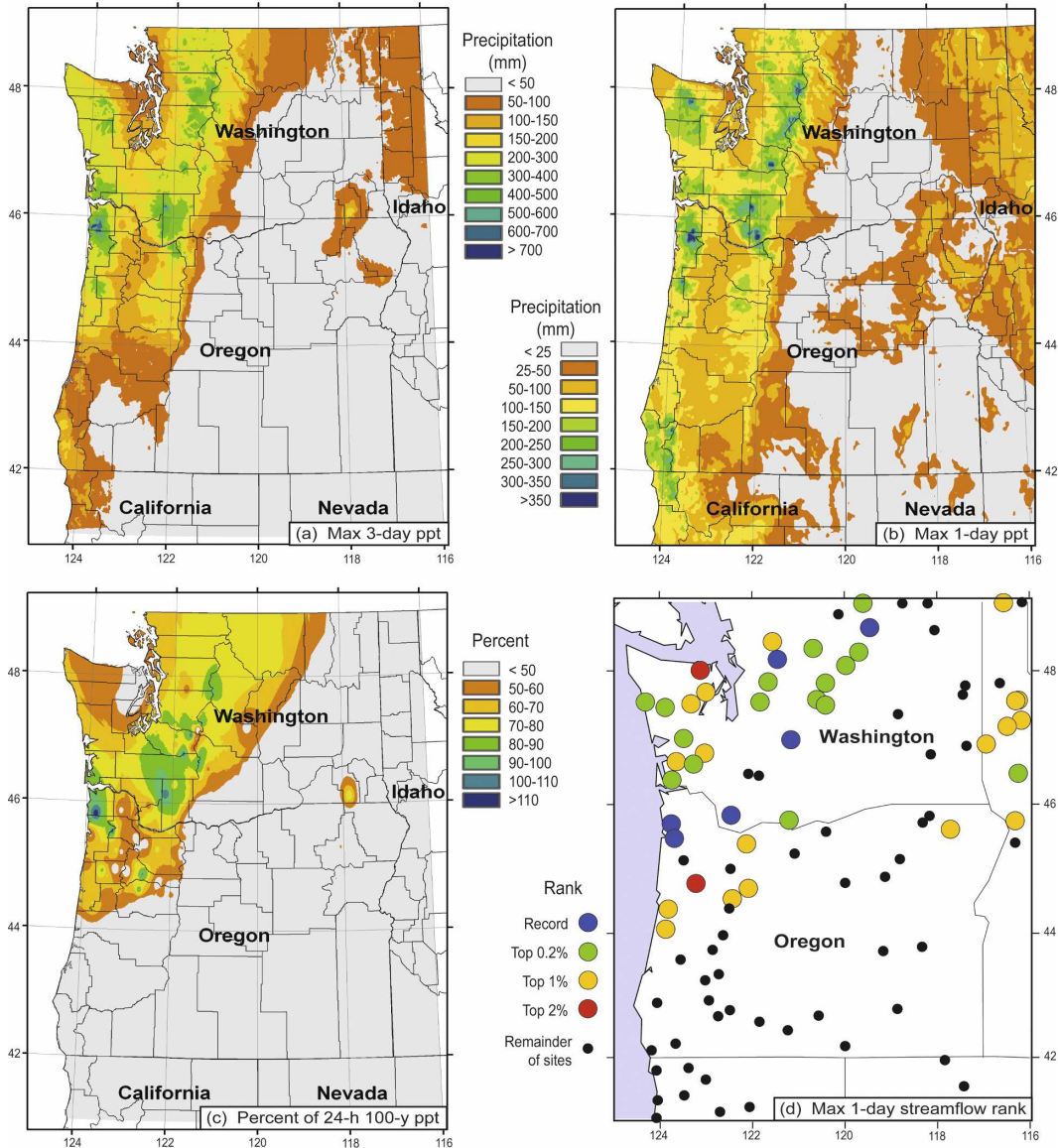


FIG. 7. Precipitation and streamflow analyses from daily surface observations recorded between 5 and 9 Nov 2006: (a) greatest 3-day precipitation totals (mm); (b) greatest 1-day precipitation totals (mm); (c) percent of the maximum 1-day precipitation totals relative to the 100-yr daily precipitation event; and (d) maximum ranking (%) of daily unregulated streamflows during the month of November for those gauges that have recorded data for ≥ 30 Novembers. These data are based on local time (add 8 h to convert to UTC).

scavenging of moisture by orographic processes as the AR penetrated inland across successive mountain ranges. A similar pattern of precipitation is observed in the maximum 1-day accumulations (Fig. 7b), with local maxima exceeding 350 mm in the Coast and Cascade Ranges, and 450 mm of rain reported in Mt. Rainier National Park over a 36-h period on 6-7 November. The single-day totals surpassed 70% of the 24-h, 100-yr precipitation event (Fig. 7c) over broad regions of these

two ranges, and they exceeded 100% in northern Oregon's Coast Range and southern Washington's Cascades. The extreme character of these precipitation accumulations is consistent with the extreme IWV and IVT observed in the landfalling AR within 1000 km of the coast (IWV > 5 cm in Fig. 4a, and IVT > 1300 kg s⁻¹ m⁻¹ in Fig. 4b).

In response to the heavy rainfall (Figs. 7a-c) and high melting levels (Figs. 6g,h) brought by the landfalling

AR of 6–7 November, most of the streams draining the Coast and Cascade Ranges in Washington and northern Oregon yielded maximum 1-day flows among the top 1% of those observed historically for November (Fig. 7d). Many of the streams were in the top 0.2%, and six gauges recorded all-time record flows for November. The widespread flooding and associated debris flows (e.g., Fig. 1) yielded significant regionwide damage on the order of \$50 million (NCDC 2006). Fortunately, no lives were lost. It should be noted that historically large 1-day flows topping 1% were also observed in the interior ranges.

4. Satellite-based COSMIC sounding analysis

Given the high-impact character of the landfalling AR in early November 2006, coupled with the fact that satellite-based COSMIC GPS RO soundings had been available for only a short time previously, we deemed this AR to be a good test case for assessing the ability of the COSMIC dataset to capture noteworthy, regularly occurring mesoscale weather phenomena over the otherwise data-sparse Pacific Ocean. The COSMIC dataset will be evaluated using two complementary methods: with compositing and via a detailed cross-section analysis.

a. Composite soundings

Figure 8 shows the locations of COSMIC soundings used to construct composite soundings north of, within, and to the south of the AR. SSM/I IWV satellite imagery served as a guide to determine the AR-relative positions of the soundings (using SSM/I IWV > ~2 cm as a key AR criterion; Ralph et al. 2004). These soundings spanned 2 days, from 0332 UTC 6 November to 0845 UTC 8 November 2006, during which time the AR propagated slowly southeastward. Hence, some overlap is seen in the positions of soundings within the AR and those to its north. There were a total of 30, 20, and 16 soundings north of the AR, within it, and to its south, respectively (see Tables 2–4). The solid-colored circles in Fig. 8 correspond to the average or centroid positions of the composite soundings (also given numerically in Tables 2–4).

Composite COSMIC soundings of temperature and dewpoint temperature are presented on a skew T -log p diagram in Fig. 9, as are their IWV values. These soundings, and the differences between them, exhibit a variety of characteristics that typify ARs and their surroundings. For example, the mean IWV within the AR is 3.61 cm, consistent with the large IWV contents observed in the AR by SSM/I and, thus, supportive of the

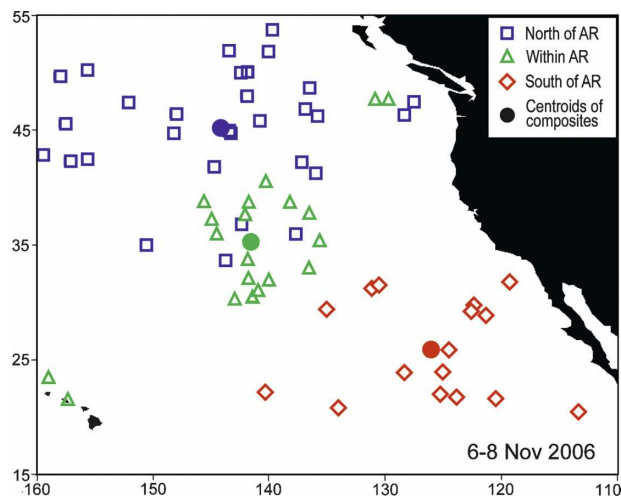


FIG. 8. Locations of COSMIC soundings between 0332 UTC 6 Nov and 0845 UTC 8 Nov 2006 (open symbols). The color coding denotes the positions of these soundings relative to the landfalling AR (blue: north of AR; green: within AR; red: south of AR). Composite SSM/I IWV satellite images starting with the 6 Nov morning composite and ending with the 8 Nov morning composite were used as a guide to determine the AR-relative positions of the soundings. Each solid-colored circle corresponds to the centroid position of the respective composite sounding.

highly favorable COSMIC-SSM/I IWV comparisons reported over the eastern North Pacific by Wick et al. (2008). Much drier mean IWVs were observed south and north of the AR (1.66 and 1.24 cm, respectively); the difference between these values reflects the expected poleward decrease in background moisture (e.g., Peixoto and Oort 1992). As anticipated, the composite sounding south of the AR is the warmest of the three in the lower and middle troposphere, and it has the highest tropopause (~180 hPa). Enhanced stability centered at ~900 hPa quite likely corresponds to the trade wind inversion, while warm and dry conditions above are suggestive of Hadley subsidence. Farther north, the sounding within the AR below ~500 hPa is cooler (by as much as ~6°C), is much closer to saturation, and exhibits a moist adiabatic profile in an environment where clouds and precipitation typically occur in conjunction with cold-frontal forcing. The tropopause is also somewhat lower (~230 hPa), as expected. Finally, the composite sounding on the north side of the AR is much colder throughout the depth of the troposphere than the other two (by as much as ~15°–20°C), and the tropopause is the lowest of the three soundings (~330 hPa), all consistent with post-cold-frontal conditions. In addition, a well-mixed boundary layer is evident between the ocean surface and ~820 hPa, indicative of upward sensible heat transfer from the relatively

TABLE 2. Locations, dates, times, IWV, and minimum radio occultation altitudes of COSMIC soundings used to construct composite thermodynamic soundings on the north side of the atmospheric river of 6–8 Nov 2006. These soundings utilized NCEP's GFS global model analyses for the first guess.

Sounding No.	Lat (°N)	Lon (°W)	Date	Time (UTC)	IWV (cm)	Min occultation altitude (m)
1	42.358	157.581	6 Nov 2006	0816	1.226	424
2	45.603	158.028	6 Nov 2006	0827	1.172	837
3	46.250	136.043	6 Nov 2006	0937	2.158	1048
4	51.880	140.375	6 Nov 2006	1855	1.700	125
5	50.264	156.087	7 Nov 2006	0354	0.889	327
6	41.888	145.091	7 Nov 2006	0423	1.494	475
7	48.744	136.722	7 Nov 2006	0446	1.532	99
8	48.015	142.250	7 Nov 2006	0455	1.164	26
9	47.531	127.658	7 Nov 2006	0456	2.470	120
10	49.722	158.446	7 Nov 2006	0548	0.850	672
11	50.087	142.073	7 Nov 2006	0550	1.006	428
12	45.030	143.769	7 Nov 2006	0631	1.364	2
13	42.255	137.367	7 Nov 2006	0732	2.199	295
14	35.058	150.946	7 Nov 2006	1950	1.103	68
15	41.325	136.232	7 Nov 2006	2216	1.423	120
16	42.540	156.079	7 Nov 2006	2357	0.970	613
17	53.807	139.995	8 Nov 2006	0302	0.836	341
18	51.895	143.747	8 Nov 2006	0330	0.819	1150
19	44.798	143.629	8 Nov 2006	0358	1.051	142
20	44.811	148.579	8 Nov 2006	0408	0.989	346
21	35.975	137.979	8 Nov 2006	0424	1.518	336
22	33.692	144.013	8 Nov 2006	0435	1.464	257
23	42.880	159.927	8 Nov 2006	0524	1.068	598
24	46.472	148.376	8 Nov 2006	0524	0.800	20
25	50.053	142.710	8 Nov 2006	0534	0.860	2
26	36.882	142.702	8 Nov 2006	0600	0.909	443
27	45.857	141.091	8 Nov 2006	0608	1.139	302
28	47.433	152.546	8 Nov 2006	0633	0.653	330
29	46.366	128.490	8 Nov 2006	0705	1.259	1
30	46.883	137.112	8 Nov 2006	0845	1.161	446
Avg	45.212	144.521			1.242	346

warm ocean surface to the comparatively cold air mass behind the cold front.

The composite COSMIC soundings are also presented in Fig. 10, where zoomed-in profiles of potential temperature (θ), equivalent potential temperature (θ_e), water vapor specific humidity (SH), and relative humidity (RH) extend upward to 6 km. These profiles quantify much of what was discussed in the previous paragraph. In addition, they show that the composite AR profile is considerably moister than those on its flanks, both from an absolute perspective (Fig. 10c) and with respect to RH (Fig. 10d). The composite SH and RH profiles also reveal that the absolute moisture content is comparable north and south of the AR above ~ 800 m MSL, even though the RH is much larger north of the AR because of colder conditions there. Enhanced values of SH below 800 m MSL on the south side of the AR point toward boundary layer moistening from the warm underlying sea surface in an otherwise dry air mass. Finally, profiles of the percentage of avail-

able RO data points (Fig. 10e) that were available for the COSMIC retrievals reveal complete coverage in all three composite soundings above 2 km MSL and 50%–80% coverage as far down as 500 m MSL. The most important vertical structures all resided above this shallow 500-m layer. The lowest altitude at which the RO data were available for each COSMIC sounding⁵ is provided in Tables 2–4.

⁵ The lowest altitude is determined based on fading of the amplitude of the RO signal transformed by the RA-HO method, which is related to either the shadowing of the RO signal by the earth's surface or loss of signal in the GPS receiver because of other reasons. Given the fact that the vertical resolution of the GPS RO technique is only ~ 20 – 30 m near the surface (Gorbunov et al. 2004), altitudes lower than a few tens of meters above the surface have no physical meaning in the retrieval. However, relative to the information contained in the entire sounding, this error is not significant, and we choose to neglect it, by using the profile down to the altitude as determined from the RA-HO transformed amplitude.

TABLE 3. Locations, dates, times, IWV, and minimum radio occultation altitudes of COSMIC soundings used to construct composite thermodynamic soundings within the atmospheric river of 6–8 Nov 2006. These soundings utilized NCEP's GFS global model analyses for the first guess.

Sounding No.	Lat (°N)	Lon (°W)	Date	Time (UTC)	IWV (cm)	Min occultation altitude (m)
1	47.751	130.989	6 Nov 2006	0332	3.621	334
2	37.842	136.787	6 Nov 2006	0428	3.584	362
3	38.835	142.029	6 Nov 2006	0438	4.544	27
4	38.856	145.893	6 Nov-2006	0459	3.085	214
5	47.754	129.853	6 Nov 2006	0509	3.564	201
6	40.671	140.533	6 Nov 2006	0604	3.620	14
7	37.774	142.305	6 Nov 2006	0744	4.669	2
8	38.863	138.437	6 Nov 2006	0745	4.028	1095
9	37.284	145.261	6 Nov 2006	0800	3.756	2
10	33.819	142.094	7 Nov 2006	0438	4.378	680
11	36.117	144.803	7 Nov 2006	0446	2.663	3
12	30.577	141.684	7 Nov 2006	0450	2.779	1
13	32.165	142.059	7 Nov 2006	0615	3.392	901
14	23.613	159.473	7 Nov 2006	0708	4.380	447
15	33.111	136.786	7 Nov 2006	0719	2.468	600
16	32.068	140.233	7 Nov 2006	0719	3.591	656
17	30.405	143.224	7 Nov 2006	1938	4.686	3
18	35.487	135.881	7 Nov 2006	2214	3.019	163
19	31.115	141.177	8 Nov 2006	0425	3.005	1096
20	21.591	157.812	8 Nov 2006	0603	3.361	1913
Avg	35.285	141.866			3.610	436

Figure 10 also displays composite dropsonde profiles from Ralph et al. (2005b), because they serve as a useful baseline comparison with the composite COSMIC soundings within the November 2006 AR. The Ralph et al. (2005b) composites are composed of 17 soundings collected from NOAA P-3 research aircraft within the pre-cold-frontal low-level jet (LLJ) of 17 different win-

tertime extratropical cyclones over the eastern North Pacific during CALJET and PACJET. The prefrontal LLJ typically coincides with the region in storms where ARs reside. The vertical-structure characteristics of the composites from the P-3 and from COSMIC within the AR are quite similar, with the acknowledgment that significant offsets were observed. For example, the θ

TABLE 4. Locations, dates, times, IWV, and minimum radio occultation altitudes of COSMIC soundings used to construct composite thermodynamic soundings on the south side of the atmospheric river of 6–8 Nov 2006. These soundings utilized NCEP's GFS global model analyses for the first guess.

Sounding No.	Lat (°N)	Lon (°W)	Date	Time (UTC)	IWV (cm)	Min occultation altitude (m)
1	31.590	130.698	6 Nov 2006	0512	1.424	406
2	21.805	123.969	6 Nov 2006	1804	1.603	352
3	25.960	124.612	6 Nov 2006	1815	1.372	973
4	31.800	119.275	7 Nov 2006	0415	1.386	125
5	29.417	135.269	7 Nov 2006	0448	1.551	143
6	22.015	125.359	7 Nov 2006	1800	1.831	1272
7	24.004	125.124	7 Nov 2006	1812	1.355	814
8	20.873	134.233	7 Nov 2006	1834	1.839	74
9	29.265	122.674	7 Nov 2006	1837	1.618	531
10	29.808	122.429	7 Nov 2006	2211	1.911	1397
11	20.479	113.322	8 Nov 2006	0313	1.587	1895
12	28.922	121.379	8 Nov 2006	0342	1.615	811
13	31.305	131.356	8 Nov 2006	0351	1.477	308
14	21.653	120.496	8 Nov 2006	0405	1.253	873
15	22.232	140.604	8 Nov 2006	0709	2.316	389
16	23.922	128.480	8 Nov 2006	0839	2.459	1436
Avg	25.941	126.205			1.662	737

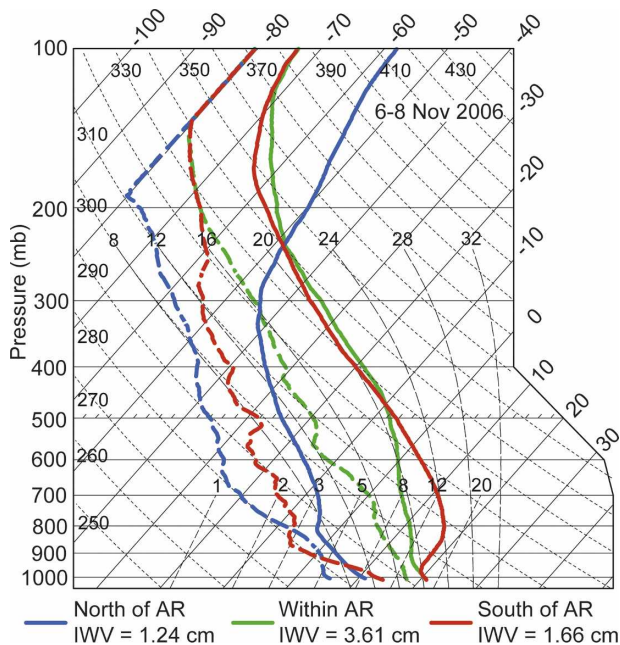


FIG. 9. Skew T - $\log p$ profiles of temperature (solid) and dew-point temperature (dashed) for the composite COSMIC soundings located north of the AR (blue), within the AR (green), and south of the AR (red) for the period 6–8 Nov 2006.

profiles (Fig. 10a) exhibit similar lapse rates, as do the θ_e profiles (Fig. 10b), despite the fact that the intense AR of November 2006 was 5–10 K warmer in θ and 15–20 K warmer in θ_e than the 17-case dropsonde composite. Similarly, the SH profiles (Fig. 10c) possess comparable slopes, even though the moisture content was much larger (by as much as $\sim 4 \text{ g kg}^{-1}$) within the November 2006 AR. Finally, the RH profiles (Fig. 10d) within AR conditions are alike, both with respect to slope and absolute value. These comparisons demonstrate further that the COSMIC soundings provide a realistic portrayal of the AR environment.

A diagnostic analysis of the composite soundings is presented in Fig. 11. Fig. 11a,b show profiles of the dry and saturated (i.e., moist) Brunt–Väisälä (BV) frequency, while Fig. 11c illustrates the vertical displacement required for each range gate to reach the lifted condensation level (LCL). We used the Durran and Klemp (1982) formulation to calculate moist BV. The dry BV for all three composite COSMIC soundings shows stable conditions, except in the lowest $\sim 200 \text{ m}$ MSL to the north of the AR where sensible heat transfer from the ocean surface was quite likely the largest of the three regimes. Below $\sim 2 \text{ km}$ MSL, the mean dry stability is weakest to the north of the AR (for the reason cited above) and strongest to the south of the AR (a manifestation of the trade wind inversion).

Aloft, the magnitude of the dry stratification in the three COSMIC soundings is similar. In contrast to the stable conditions portrayed in the dry BV profiles, the moist BV shows sublayers of instability below 2 km MSL for all COSMIC soundings. Above 2 km MSL, the AR sounding remains roughly moist-neutral upward through at least 4 km MSL in an environment that is often characterized by frontally forced ascent. The other COSMIC soundings are stable in an absolute sense above 2 km MSL.

With the nearly saturated conditions observed below 2 km MSL in the composite COSMIC sounding within the AR (Fig. 10d), only several hundred meters of ascent are required to reach saturation (Fig. 11c), which is smaller than the $\sim 1\text{-km}$ height of the mountains providing the orographic lift in the Pacific Northwest. This, coupled with the deep-layer moist-neutral (and moist unstable) stratification extending up to 4 km MSL, yields conditions highly conducive to orographic precipitation enhancement. Generally similar conditions define the region north of the AR, although the moist instability is only 2 km deep (Fig. 11b) and the absolute moisture content is less than half that found in the AR (Fig. 10c). Hence, orographic precipitation enhancement should be less pronounced north of the AR, at least from a thermodynamic perspective. Significantly, the region south of the AR is quite different from its northern counterparts. Specifically, above the strongly capped boundary layer (i.e., above $\sim 750 \text{ m}$ MSL), 2–3 km of lift is required for the dry air mass to reach saturation. Consequently, this region should not expect significant orographic precipitation enhancement. It should be noted that, given the close agreement in Fig. 10 between the composite COSMIC sounding within the AR and the composite dropsonde sounding for similar conditions, it is not surprising that the corresponding BV and vertical-displacement profiles in Fig. 11 also closely track one another.

In an attempt to establish that the COSMIC retrievals yield beneficial new information rather than simply mirroring the numerical model conditions, composite soundings of RH from the GFS and ECMWF model analyses and from the COSMIC satellites (using the models as first guess) are shown in Fig. 12. These composites are stratified by position relative to the AR. The greatest model uncertainty is found within the important mesoscale corridor of the AR rather than to its north or south. In all three regions, the COSMIC soundings converge toward each other relative to their model counterparts, although this is most evident within the AR. In addition, vertical-structure detail is gained in the COSMIC soundings, especially in AR conditions. The majority of these improvements comes

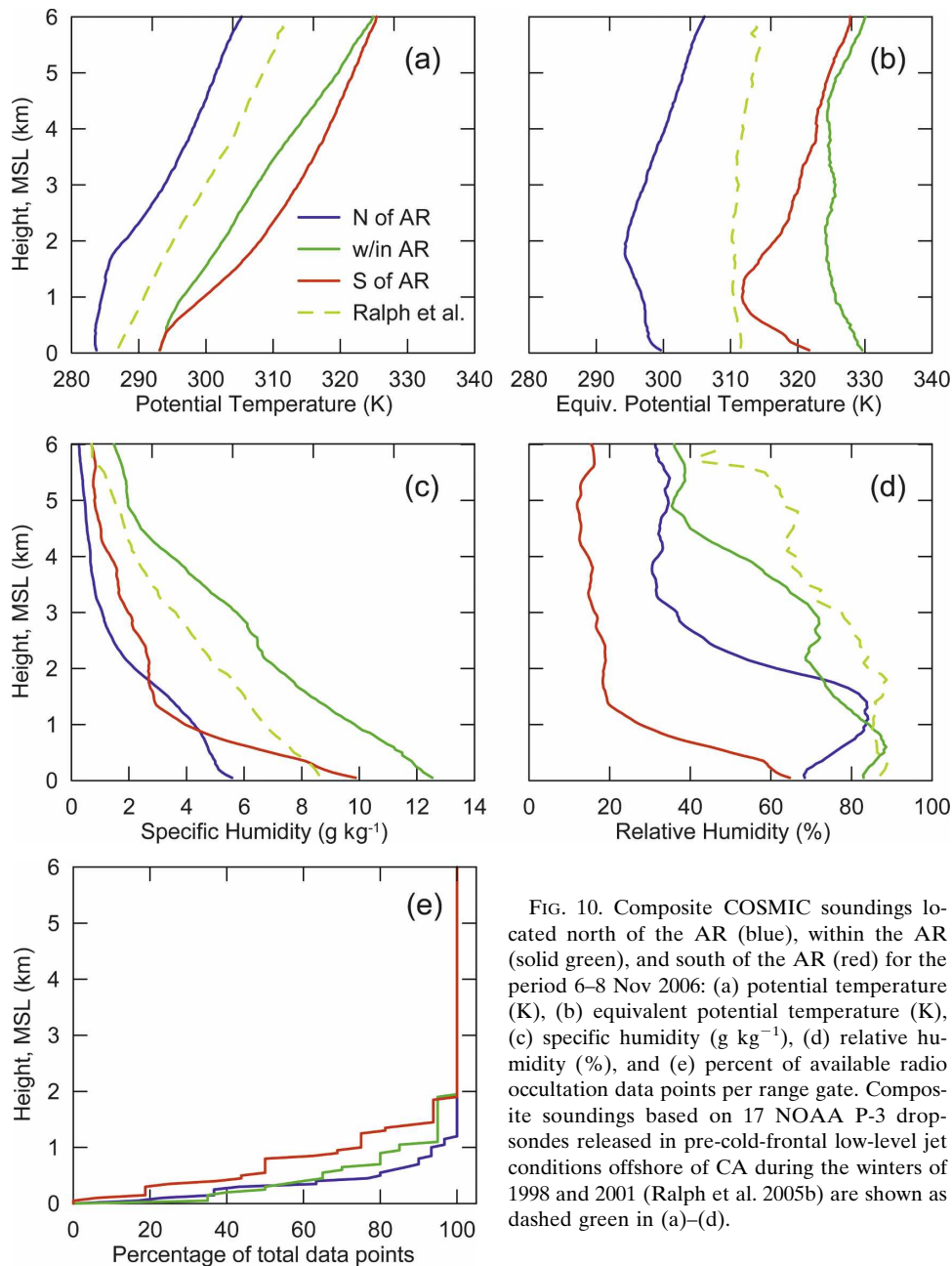


FIG. 10. Composite COSMIC soundings located north of the AR (blue), within the AR (solid green), and south of the AR (red) for the period 6–8 Nov 2006: (a) potential temperature (K), (b) equivalent potential temperature (K), (c) specific humidity (g kg^{-1}), (d) relative humidity (%), and (e) percent of available radio occultation data points per range gate. Composite soundings based on 17 NOAA P-3 dropsondes released in pre-cold-frontal low-level jet conditions offshore of CA during the winters of 1998 and 2001 (Ralph et al. 2005b) are shown as dashed green in (a)–(d).

from SH rather than from θ (not shown), as will be revealed in the context of a cross-section analysis presented in section 4b.

b. Cross-section perspective

In section 4a, we employed a compositing approach to showcase the observing capabilities of the new COSMIC sounding dataset during the landfall of the intense AR of early November 2006. Here, we will further explore the ability of COSMIC to capture this

high-impact weather event by constructing a snapshot, $\sim 4500\text{-km}$ -long cross section through the AR (Fig. 13) using 12 soundings. The positions of the soundings relative to the AR are shown in Fig. 3, and additional relevant sounding information is given in Table 5. Eleven of these soundings were acquired within a narrow $\sim 3.5\text{-h}$ window across a 3500-km baseline between 0354 and 0732 UTC 7 November 2006. Even the fastest dropsonde aircraft cannot cover this distance in the allotted time. The twelfth sounding, taken

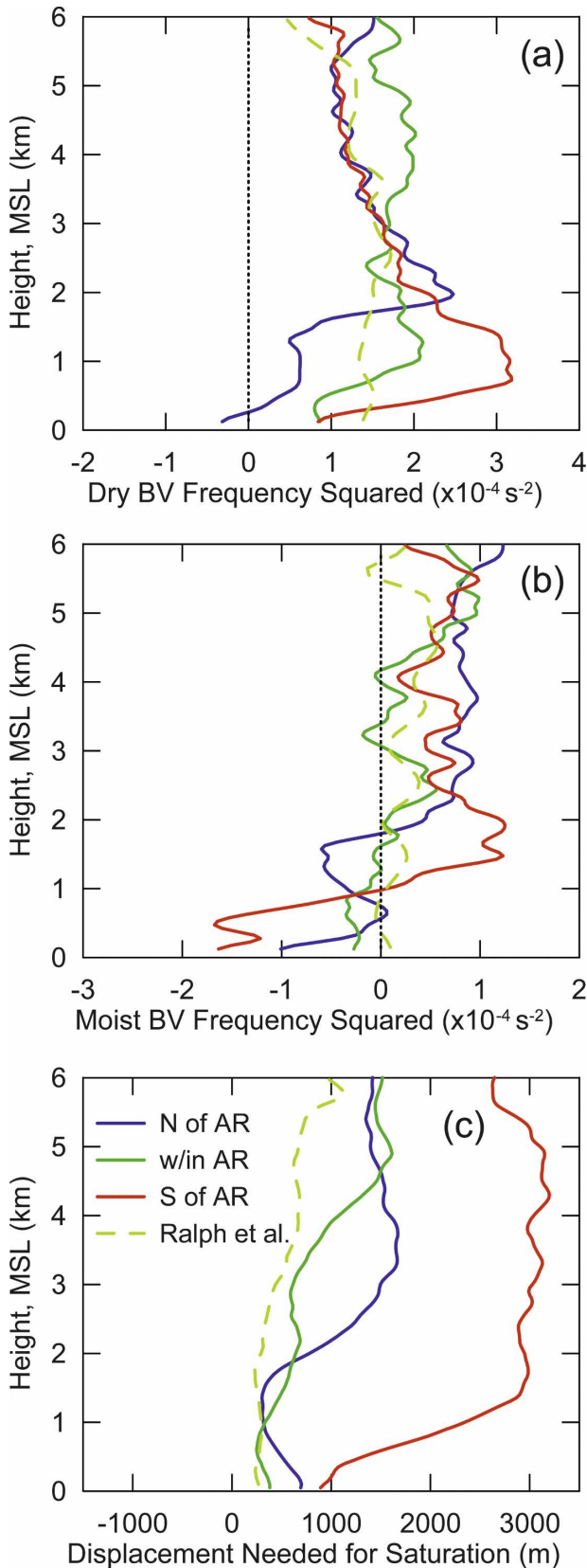


FIG. 11. As in Fig. 10, but for (a) dry Brunt-Väisälä frequency ($\times 10^{-4} \text{ s}^{-2}$); (b) moist Brunt-Väisälä frequency ($\times 10^{-4} \text{ s}^{-2}$), and (c) the vertical displacement (m) required for saturation.

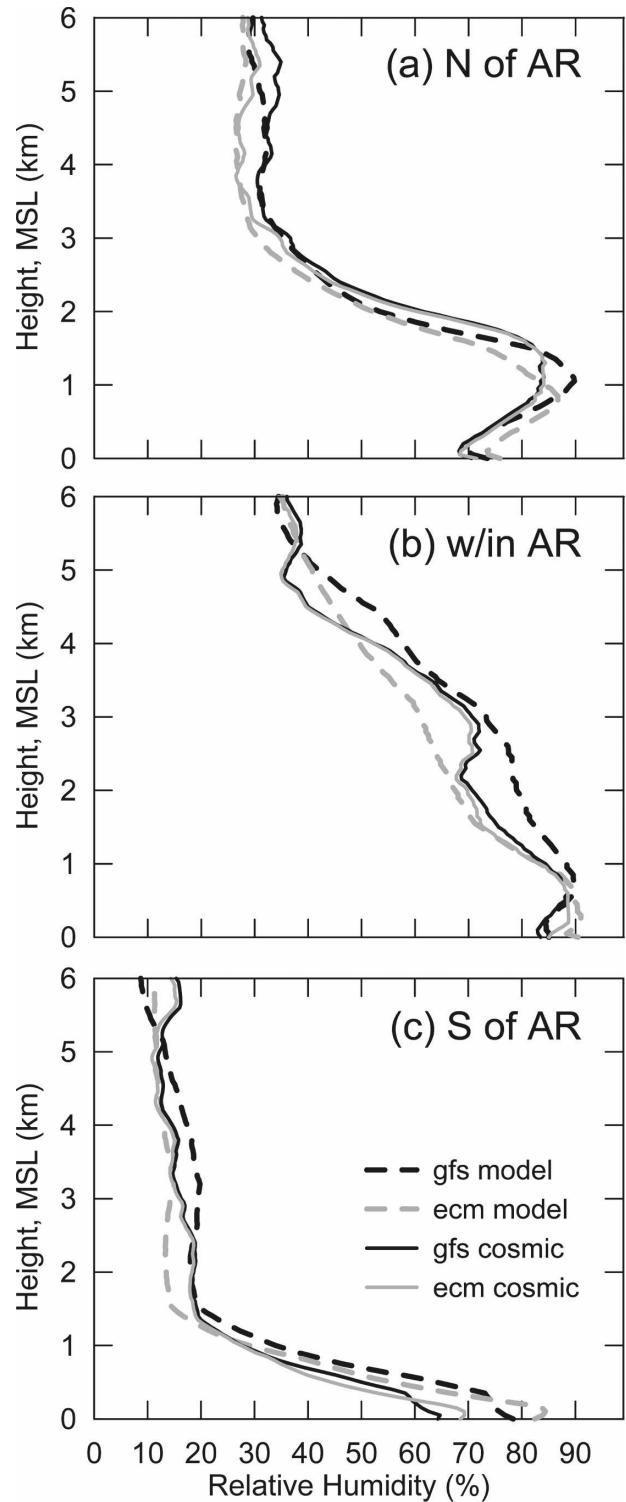


FIG. 12. Composite soundings of relative humidity (%) from the GFS model analyses (black dash), the ECMWF model analyses (gray dash), the COSMIC satellites using the GFS analyses as first guess (black solid), and the COSMIC satellites using the ECMWF analyses as first guess (gray solid) for the period 6–8 Nov 2006: (a) north of the atmospheric river, (b) within the atmospheric river, and (c) south of the atmospheric river.

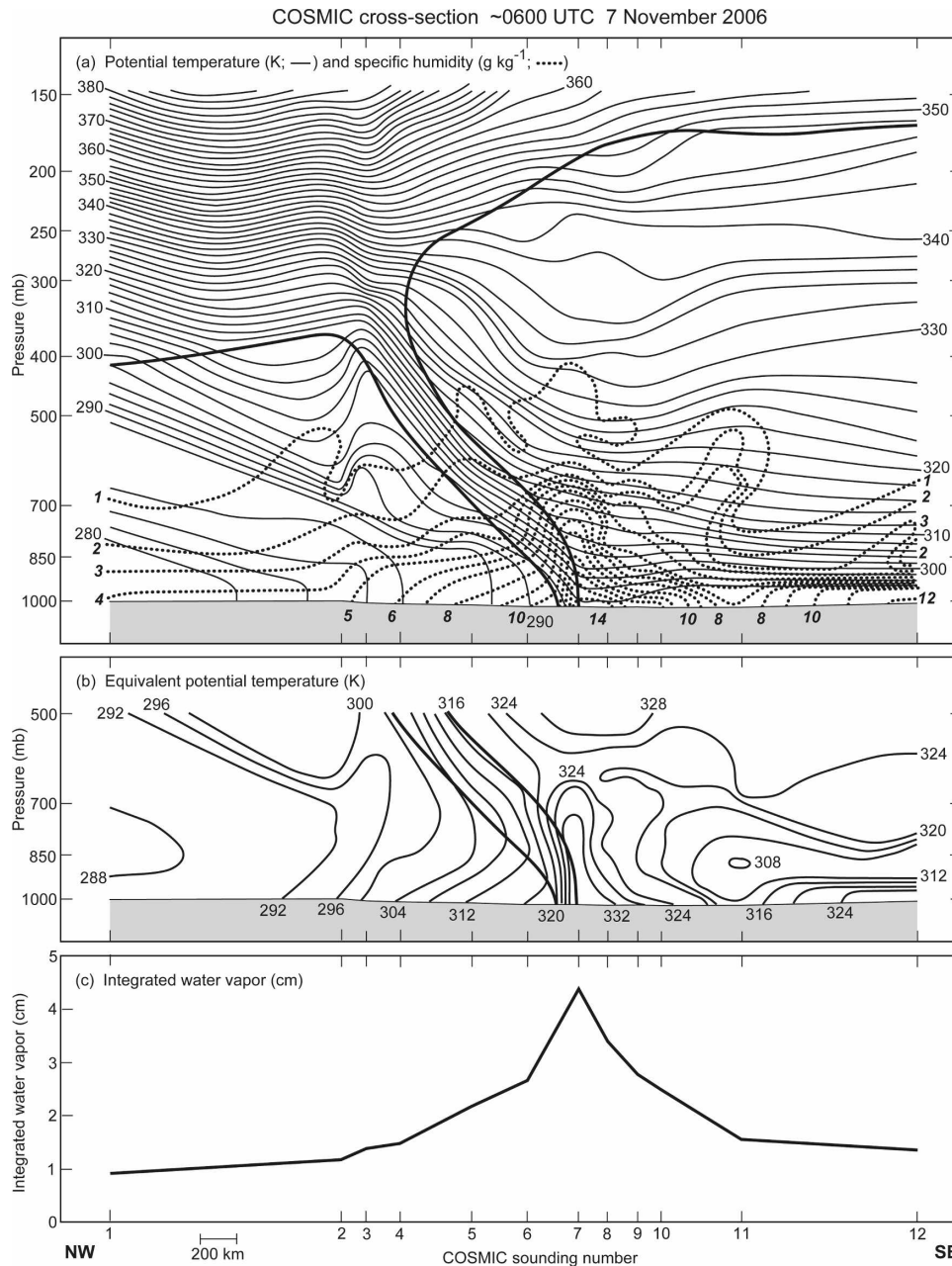


FIG. 13. Cross sections of COSMIC soundings (shown in Fig. 3 and listed in Table 5) along line NW–SE in Figs. 3 and 6e: (a) potential temperature (K, solid) and water vapor SH (g kg^{-1} ; dotted) to 150 hPa; (b) equivalent potential temperature (K) to 500 hPa; and (c) IWV (cm). Bold solid lines in (a) and (b) are frontal boundaries and the tropopause.

at 1812 UTC 7 November, is situated at the southern end of the cross section far from the AR, so its temporal mismatch relative to the others should not adversely impact the analysis.

The cross section of θ and SH (Fig. 13a) shows the vertical continuity of a polar cold front sloping north-westward from the ocean surface to the tropopause. A

concentrated band of enhanced SH ($>14 \text{ g kg}^{-1}$ near the surface) coincides with the peak value of IWV (4.38 cm; Fig. 13c) within the narrow AR near the leading edge of the front. The vertical penetration of this band implies forced ascent associated with low-level frontal convergence, consistent with the satellite rope-cloud observations in Figs. 2b,c. Ahead of the cold front, θ

TABLE 5. Locations, times (on 7 Nov 2006), IWV, and minimum radio occultation altitudes of COSMIC soundings used to construct a cross section through the atmospheric river of 7 Nov 2006 (see Fig. 13). These soundings utilized NCEP's GFS global model analyses for the first guess.

Sounding No.	Lat (°N)	Lon (°W)	Time (UTC)	IWV (cm)	Min occultation altitude (m)
1	50.264	156.087	0354	0.889	327
2	48.015	142.250	0455	1.164	26
3	45.030	143.769	0631	1.364	2
4	41.888	145.091	0423	1.494	475
5	42.255	137.367	0732	2.198	295
6	36.117	144.803	0446	2.663	3
7	33.819	142.094	0438	4.378	680
8	32.165	142.059	0615	3.392	901
9	30.577	141.684	0450	2.779	1
10	33.111	136.786	0719	2.468	600
11	29.417	135.269	0448	1.551	143
12	24.004	125.124	1812	1.355	814
Avg					356

decreases toward the southeast below ~ 750 hPa. The position of this reverse thermal gradient relative to both the front and the band of enhanced SH suggests, from a geostrophic standpoint, the presence of a pre-cold-frontal LLJ residing within the shallow moist plume, as has been observed directly in other ARs (e.g., Ralph et al. 2004, 2005b). Aloft, θ decreases to the northwest within the front and on its warm side, thus signifying the presence of an upper-tropospheric jet stream (the global reanalysis documented a 65 m s^{-1} jet stream over the AR; not shown). In the southeast portion of the cross section, coinciding sharp vertical gradients of θ and SH mark the low-level trade wind inversion.

The companion cross section of θ_e (Fig. 13b) also shows a well-defined cold front and prefrontal band of enhanced moisture penetrating vertically. Maximum θ_e content within this prefrontal plume exceeds 332 K below ~ 750 hPa, consistent with the plan-view depiction of this plume in the 925-hPa reanalysis mean field (Fig. 6e). Moist-neutral stratification characterizes this high- θ_e environment, as is also the case in the composite AR soundings (Figs. 10b and 11b). Low-level potential instability on the cold side of the front (Figs. 13a,b) is also portrayed in the composite soundings north of the AR (Figs. 10a,b). Finally, a sharp minimum in θ_e southeast of the AR at ~ 900 hPa marks the dry cap atop the trade wind inversion, comparable to that shown in the composite soundings south of the AR.

Importantly, the RO data that were used to retrieve the 12 COSMIC soundings analyzed in Fig. 13 penetrated downward to near the ocean surface in all of

those soundings. The lowest altitude of these data ranged between 1 and 901 m MSL, with an average of 356 m MSL or ~ 975 hPa (Table 5). Hence, all of the salient mesoscale structures depicted in Fig. 13 were contained within the envelope of available RO data.

In an effort to extend the discussion in section 4a that the COSMIC soundings do not mirror the numerical model analyses, differences are calculated from the 12 soundings used in the cross sections (Fig. 14). Difference fields of θ and SH between the ECMWF and GFS model soundings ($\Delta\theta_M$ and ΔSH_M , respectively) are shown in Figs. 14a,c, while difference fields of θ and SH between the COSMIC sounding retrievals using the ECMWF and GFS models as the first guess ($\Delta\theta_C$ and ΔSH_C , respectively) are given in Figs. 14b,d. Spatially coherent patterns are evident in all panels. Significantly, the largest differences are between the models ($\Delta\theta_M > 4 \text{ K}$, $\Delta SH_M < -2 \text{ g kg}^{-1}$) in the vicinity of the AR, which is an important region of mesoscale focus. Where the magnitude of the differences between the COSMIC retrievals is less than the magnitude of the differences between the model profiles, it is highly suggestive that the COSMIC RO data yielded beneficial impacts (i.e., the soundings used in Fig. 13 quite likely contain more information than the model soundings). This is particularly evident by comparing the ΔSH panels, where the COSMIC differences are substantially less than their model counterparts, especially in the low-level prefrontal environment where the AR resides. The COSMIC potential temperature differences are also generally less than their model counterparts, but mainly below ~ 700 hPa. Overall, the differences in the COSMIC fields are reduced most significantly (relative to the model fields) in the vicinity of the AR, thus revealing that the COSMIC retrievals provided the greatest benefit in the key mesoscale region under consideration. This is consistent with the composite results in Fig. 12. Furthermore, it is noteworthy that the COSMIC SH soundings converge more strongly toward each other than the COSMIC θ soundings (e.g., ΔSH_C is much smaller than $\Delta\theta_C$), especially in the region of the AR, thus implying that the COSMIC soundings provide greater benefit in defining crucial moisture (rather than temperature) structures in the vicinity of the AR.

Expanding on the previous discussion, differences are also calculated from composites of the 12 cross-section soundings (Fig. 15). The magnitude of the composite differences between the COSMIC retrievals ($\Delta\theta_C$, ΔSH_C) is significantly less than the magnitude of the differences between the model profiles ($\Delta\theta_M$, ΔSH_M) in the lowest 2.5 km, where 75% of the column-integrated horizontal water vapor transport occurs, on

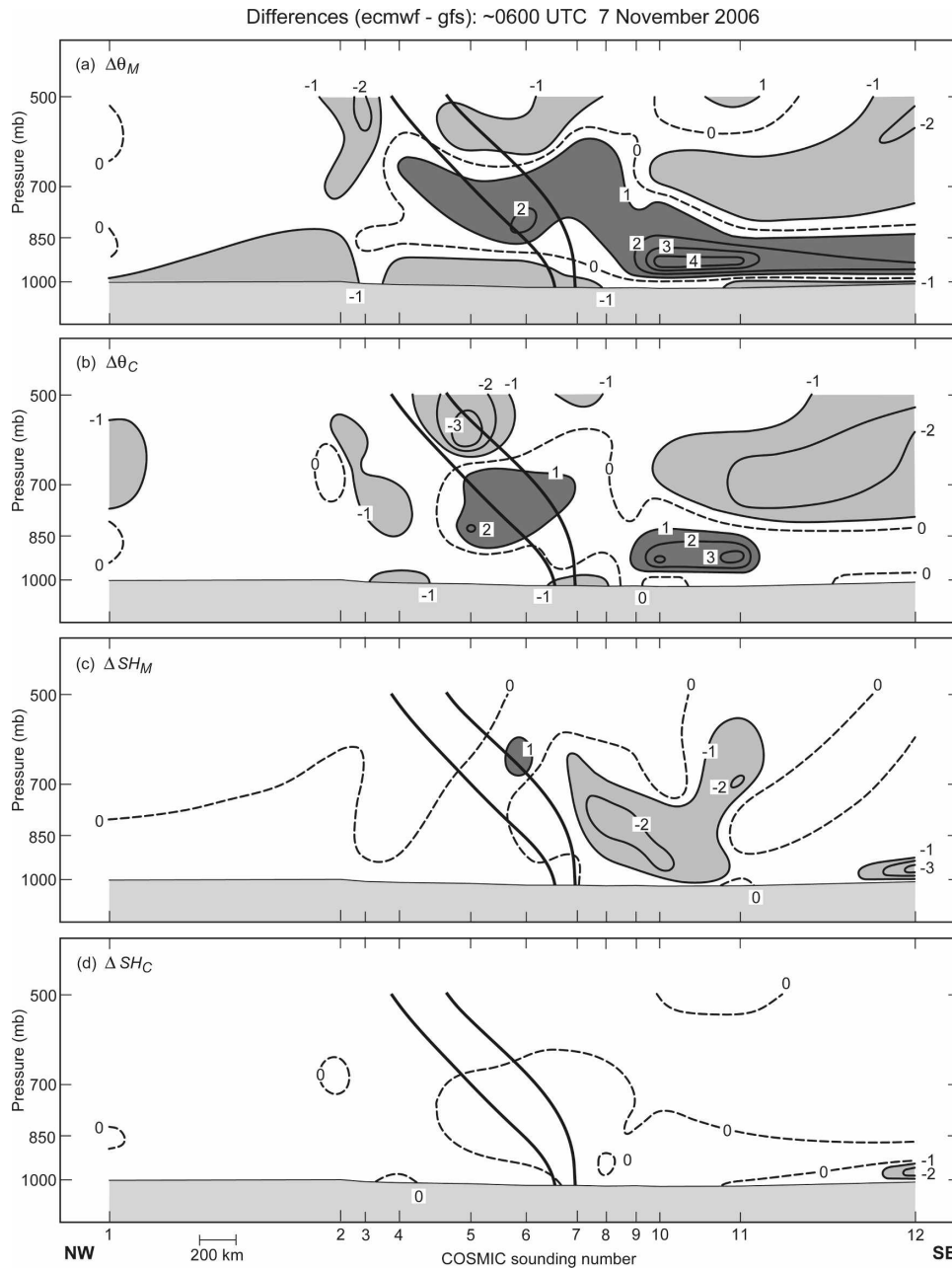


FIG. 14. As in Fig. 13b, but for difference fields of (a) potential temperature between the ECMWF and GFS model analysis soundings ($\Delta\theta_M$; K), (b) potential temperature between the COSMIC soundings using the ECMWF and GFS model analyses as the first guess ($\Delta\theta_C$; K), (c) specific humidity between the ECMWF and GFS model analysis soundings (ΔSH_M ; g kg^{-1}), and (d) specific humidity between the COSMIC soundings using the ECMWF and GFS model analyses as the first guess (ΔSH_C ; g kg^{-1}). Dark gray shading highlights differences exceeding 1 unit, while light shading portrays differences less than -1 unit.

average, in ARs (Ralph et al. 2005b). In this layer, the mean absolute values of $\Delta\theta_C$ and $\Delta\theta_M$ (i.e., the layer-mean absolute differences) are 0.39 and 0.60 K, respectively. Alternately stated, the layer-mean absolute value of $\Delta\theta_C$ in the crucial layer where ARs are focused is 35% less than that of $\Delta\theta_M$. The results for moisture

are even more encouraging. Namely, the layer-mean absolute value of ΔSH_C (0.07 g kg^{-1}) is 0.43 g kg^{-1} less than that of ΔSH_M (0.50 g kg^{-1}), or an 86% reduction. This decrease also represents 7.7% of the average SH in that layer. Above 2.5 km, the COSMIC retrievals bring the soundings closer together, on average,

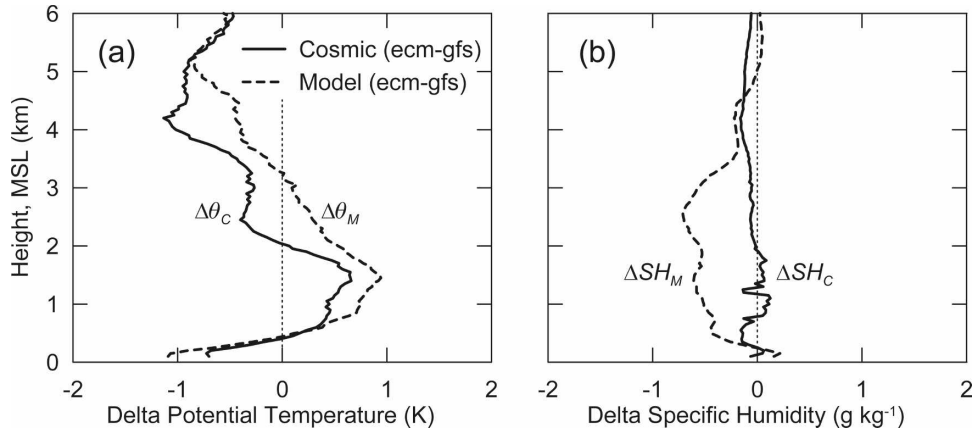


FIG. 15. Differences in (a) potential temperature (K), and (b) specific humidity (g kg^{-1}), between composites of the 12 soundings used to construct the cross sections in Figs. 13 and 14. The solid lines show the differences between the COSMIC sounding composites using the ECMWF and GFS analyses as the first guess, and the dashed lines portray the model differences between the ECMWF and GFS analyses.

through 4.5 km for SH, but that some levels show increases in the differences for θ . In other words, the COSMIC profiles show greater agreement with one another for SH at all levels below 4.5 km than do the model soundings, while for θ , this is only true up to 2.5 km MSL.

Relative to the operational models, the COSMIC soundings offer greater vertical resolution in the lower troposphere (e.g., Sokolovskiy et al. 2006), where water vapor is concentrated. For this reason, and the reasons described in the two previous paragraphs, it is evident that the mesoscale structures analyzed in the cross section (Fig. 13) were resolved partly due to the inclusion of COSMIC RO data. While the model analyses contained the primary polar front and associated atmospheric river without the use of COSMIC soundings, key mesoscale characteristics of the AR (e.g., its position, water vapor content, amplitude, orientation, etc.) became better defined. It is expected that, through assimilation of the COSMIC measurements (Kuo et al. 2000), these mesoscale features will be better represented and will ultimately reduce diagnostic and forecast errors associated with ARs over remote oceanic regions. Although the analyses presented here are supportive of this conclusion, further work needs to be done to include many more events and to diagnose specific error reductions, possibly using dropsondes deployed in these remote areas using aircraft.

5. Conclusions

a. Diagnosis of atmospheric river conditions

An intense storm was examined over the eastern North Pacific Ocean that ultimately made landfall

across the Pacific Northwest on 6–8 November 2006. This event was characterized by an extended period of heavy rainfall that set records and, at some locations, exceeded 100-yr precipitation thresholds for 24-h periods. The warmth of this event was also remarkable and contributed to anomalously high snow-melting levels that contributed to widespread flooding and damaging debris flows.

Using SSM/I satellite observations of IWV, as well as reanalysis data, it was found that a strong AR was present during this case. To quantify the amplitude of this AR, a method was developed that concluded this AR was among the most intense of 119 AR days observed over 9 yr in this region. It was the strongest in terms of water vapor transport amplitude derived from reanalysis data, and was tied for second in the direct observations of maximum IWV within 1000 km of the coast as measured by SSM/I satellite data. This study adds further evidence [to the seven cases shown in Ralph et al. (2006) for flooding on California's Russian River] that ARs are critical contributors to West Coast extreme precipitation and flooding events. In addition, it extends the work of Ralph et al. (2006) by showing this is true for a more northern latitude, and by developing a method that ranks individual events (using the catalog developed by Neiman et al. 2008). Discussions with operational weather forecasters in the region, including those responsible for quantitative precipitation forecasts (QPF), suggest that this method can be valuable in operational forecasting.

b. Evaluation of a new satellite dataset: COSMIC

The intense AR of November 2006 was used to evaluate the detailed vertical-profiling capabilities of

the new satellite-based COSMIC GPS radio occultation sounding technique within high-impact, regularly occurring mesoscale weather phenomena over otherwise data-sparse oceanic regions. Because this study describes the first phenomenological-based COSMIC evaluation of its kind, this AR was deemed an excellent test case owing to its large signal-to-noise ratio (i.e., its well-defined character). The successful evaluation of this strong event (as is summarized below) lays the groundwork for future phenomenological assessments of weaker ARs and composites of ARs to determine whether or not COSMIC can adequately capture the full spectrum of this class of high-impact weather events. The COSMIC soundings taken within the AR environment of November 2006 were assessed for their realism, based on the meteorological context provided by the SSM/I and reanalysis datasets and on comparisons made between the COSMIC soundings and NOAA P-3 dropsondes released within other ARs during earlier research missions. The COSMIC dataset was evaluated using two complementary methods: with compositing and via a detailed cross-section analysis.

The retrieval of temperature and moisture soundings from COSMIC observations must be initialized with a first-guess profile such as from numerical weather prediction model analyses. For this study, the first-guess source was obtained primarily from NCEP's GFS model. Relevant offshore COSMIC soundings on 6–8 November 2006 were grouped into three clusters for compositing: those north of the AR (30 soundings), those within the AR (20 soundings), and those to its south (16 soundings). These groupings were made possible by referring to the twice-daily SSM/I IWV images for guidance. The composite soundings for these three regions exhibited vertical-structure characteristics of temperature and moisture that were meteorologically consistent with global reanalysis fields of this case and with earlier case study and composite results based on dropsondes released in ARs during the CALJET and PACJET field programs. In addition, a curtain of 12 offshore COSMIC soundings through the AR of November 2006 yielded cross-sectional thermodynamic structures that were consistent with the composite COSMIC soundings of this event. This cross section also provided a thermodynamic description of the AR comparable in detail to previous aircraft-based dropsonde surveys of ARs over the eastern North Pacific Ocean (e.g., Ralph et al. 2004).

Because the COSMIC soundings involve the use of a first-guess from an operational numerical model, it was necessary to evaluate how the COSMIC soundings differed from those of either the GFS or ECMWF model

soundings. In contrast to the model soundings, the COSMIC soundings converged on a common solution for specific humidity, especially below ~ 4.5 km MSL, independent of which first guess was used. This was also the case to a lesser extent for potential temperature below ~ 2.5 km MSL, where $\sim 75\%$ of the water vapor transport within ARs typically occurs. These comparisons are distinct from that of vertically integrated variables assessed in Wick et al. (2008), who showed that the COSMIC-derived IWV was valuable in evaluating the performance of several competing algorithms used for processing SSM/I radiance data into IWV and cloud liquid water.

The satellite-based COSMIC soundings represent a new, global thermodynamic and moisture dataset with high vertical resolution in the lower and middle troposphere. The enhanced vertical resolution at lower levels—atypical of most satellite sounding products—is especially useful, because it can readily document atmospheric rivers and other high-impact mesoscale weather phenomena that are characterized by large concentrations of low-level water vapor. Until now, soundings such as these over data-sparse regions were gathered primarily during expensive, episodic airborne-based field programs across very limited domains. Even though COSMIC soundings cannot provide wind information or, by extension, water vapor transports, they can ultimately prove indispensable in a wide array of applications ranging from data assimilation and numerical weather prediction to climate studies. Finally, by combining COSMIC retrievals with wind observations from airborne missions (either manned or unmanned), water vapor transports can be ascertained. Future studies will address the impact of these existing and potentially new observing systems on monitoring and prediction of atmospheric rivers and other comparable, high-impact mesoscale phenomena over data-sparse regions of the globe.

Acknowledgments. We thank Cathy Smith and colleagues of NOAA's Earth System Research Laboratory for developing the NCEP–NCAR reanalysis composite tools and making them available (see online at <http://www.cdc.noaa.gov/Composites/Day>). Darren Jackson of NOAA/ESRL prepared the GOES satellite imagery. Jim Adams electronically drafted the majority of the figures presented in this paper, and Allen White of NOAA/ESRL generously donated time to generate three additional figures. Sergey Sokolovskiy of UCAR/COSMIC provided valuable assistance for the revision of the paper. This work was partially funded by the National Science Foundation under Grant ATM-0410018.

REFERENCES

- Anthes, R. A., and Coauthors, 2008: The COSMIC/FORMOSAT-3 Mission: Early results. *Bull. Amer. Meteor. Soc.*, **89**, 313–333.
- Bao, J.-W., S. A. Michelson, P. J. Neiman, F. M. Ralph, and J. M. Wilczak, 2006: Interpretation of enhanced integrated water vapor bands associated with extratropical cyclones: Their formation and connection to tropical moisture. *Mon. Wea. Rev.*, **134**, 1063–1080.
- Bond, N. A., and M. A. Shapiro, 1991: Research aircraft observations of the mesoscale and microscale structure of a cold front over the eastern Pacific Ocean. *Mon. Wea. Rev.*, **119**, 3080–3094.
- Browning, K. A., 1990: Organization of clouds and precipitation in extratropical cyclones. *Extratropical Cyclones: The Erik Palmén Memorial Volume*, C.W. Newton and E. Holopainen, Eds., Amer. Meteor. Soc., 129–153.
- Carlson, T. N., 1991: *Mid-Latitude Weather Systems*. Harper-Collins, 507 pp.
- Cheng, C.-Z., Y.-H. Kuo, R. A. Anthes, and L. Wu, 2006: Satellite constellation monitors global and space weather. *Eos, Trans. Amer. Geophys. Union*, **87** (17), 166–167.
- Daly, C., R. P. Neilson, and D. L. Phillips, 1994: A statistical-topographic model for mapping climatological precipitation over mountainous terrain. *J. Appl. Meteor.*, **33**, 140–158.
- Durran, D. R., and J. B. Klemp, 1982: On the effects of moisture on the Brunt-Väisälä frequency. *J. Atmos. Sci.*, **39**, 2152–2158.
- Falvey, M., and R. Garreaud, 2007: Wintertime precipitation episodes in central Chile: Associated meteorological conditions and orographic influences. *J. Hydrometeorol.*, **8**, 171–193.
- Gorbunov, M. E., H.-H. Benzon, A. S. Jensen, M. S. Lohmann, and A. S. Nielsen, 2004: Comparative analysis of radio occultation processing approaches based on Fourier integral operators. *Radio Sci.*, **39**, RS6004, doi:10.1029/2003RS002916.
- Hollinger, J. P., J. L. Peirce, and G. A. Poe, 1990: SSM/I instrument evaluation. *IEEE Trans. Geosci. Remote Sens.*, **28**, 781–790.
- Hunter, R. D., and R. K. Meentemeyer, 2005: Climatologically aided mapping of daily precipitation and temperature. *J. Appl. Meteor.*, **44**, 1501–1510.
- Junker, N. W., R. H. Grumm, R. Hart, L. F. Bosart, K. M. Bell, and F. J. Pereira, 2008: Use of normalized anomaly fields to anticipate extreme rainfall in the mountains of northern California. *Wea. Forecasting*, **23**, 336–356.
- Kalnay, E., and Coauthors, 1996: The NCEP/NCAR 40-Year Reanalysis Project. *Bull. Amer. Meteor. Soc.*, **77**, 437–471.
- Kiladis, G. N., 1998: Observations of Rossby waves linked to convection over the eastern tropical Pacific. *J. Atmos. Sci.*, **55**, 321–339.
- Knippertz, P., 2007: Tropical-extratropical interactions related to upper-level troughs at low latitudes. *Dyn. Atmos. Oceans*, **43**, 36–62.
- Kuo, Y.-H., B. Chao, and L. Lee, 1999: A constellation of micro-satellites promises to help in a range of geoscience research. *Eos, Trans. Amer. Geophys. Union*, **80** (40), 467–471.
- , S. Sokolovskiy, R. A. Anthes, and F. Vandenberghe, 2000: Assimilation of GPS radio occultation data for numerical weather prediction. *Terr. Atmos. Oceanic Sci.*, **11**, 157–186.
- , T.-K. Wee, S. Sokolovskiy, C. Rocken, W. Schreiner, D. Hunt, and R. A. Anthes, 2004: Inversion and error estimation of GPS radio occultation data. *J. Meteor. Soc. Japan*, **82** (1B), 507–531.
- Kursinski, E. R., G. A. Hajj, K. R. Hardy, J. T. Schofield, and R. Linfield, 1997: Observing Earth's atmosphere with radio occultation measurements. *J. Geophys. Res.*, **102**, 23 429–23 465.
- Lundquist, J. D., P. J. Neiman, B. E. Martner, A. B. White, D. J. Gottas, and F. M. Ralph, 2008: Rain versus snow in the Sierra Nevada, California: Comparing Doppler profiling radar and surface observations of melting level. *J. Hydrometeorol.*, **9**, 194–211.
- McCabe, G. J., M. P. Clark, and L. E. Hay, 2007: Rain-on-snow events in the western United States. *Bull. Amer. Meteor. Soc.*, **88**, 319–328.
- Neiman, P. J., F. M. Ralph, A. B. White, D. E. Kingsmill, and P. O. G. Persson, 2002: The statistical relationship between upslope flow and rainfall in California's coastal mountains: Observations during CALJET. *Mon. Wea. Rev.*, **130**, 1468–1492.
- , B. E. Martner, A. B. White, G. A. Wick, F. M. Ralph, and D. E. Kingsmill, 2005: Wintertime nonbrightband rain in California and Oregon during CALJET and PACJET: Geographic, interannual, and synoptic variability. *Mon. Wea. Rev.*, **133**, 1199–1223.
- , F. M. Ralph, G. A. Wick, J. Lundquist, and M. D. Dettinger, 2008: Meteorological characteristics and overland precipitation impacts of atmospheric rivers affecting the West Coast of North America based on eight years of SSM/I satellite observations. *J. Hydrometeorol.*, **9**, 22–47.
- NCDC, 2006: *Storm Data*. Vol. 48, No. 11, 106 pp.
- Pandey, G. R., D. R. Cayan, and K. P. Georgakakos, 1999: Precipitation structure in the Sierra Nevada of California during winter. *J. Geophys. Res.*, **104**, 12 019–12 030.
- Peixoto, J. P., and A. H. Oort, 1992: *Physics of Climate*. American Institute of Physics, 520 pp.
- Ralph, F. M., P. J. Neiman, D. E. Kingsmill, P. O. G. Persson, A. B. White, E. T. Strem, E. D. Andrews, and R. C. Antweiler, 2003: The impact of a prominent rain shadow on flooding in California's Santa Cruz Mountains: A CALJET case study and sensitivity to the ENSO cycle. *J. Hydrometeorol.*, **4**, 1243–1264.
- , —, and G. A. Wick, 2004: Satellite and CALJET aircraft observations of atmospheric rivers over the eastern North Pacific Ocean during the winter of 1997/98. *Mon. Wea. Rev.*, **132**, 1721–1745.
- , and Coauthors, 2005a: Improving short-term (0–48 h) cool-season quantitative precipitation forecasting: Recommendations from a USWRP workshop. *Bull. Amer. Meteor. Soc.*, **86**, 1619–1632.
- , P. J. Neiman, and R. Rotunno, 2005b: Dropsonde observations in low-level jets over the northeastern Pacific Ocean from CALJET-1998 and PACJET-2001: Mean vertical-profile and atmospheric-river characteristics. *Mon. Wea. Rev.*, **133**, 889–910.
- , —, G. A. Wick, S. I. Gutman, M. D. Dettinger, D. R. Cayan, and A. B. White, 2006: Flooding on California's Russian River: The role of atmospheric rivers. *Geophys. Res. Lett.*, **33**, L13801, doi:10.1029/2006GL026689.
- Rhea, J. O., 1978: Orographic precipitation model for hydrometeorological use. Ph.D. dissertation, Dept. of Atmospheric Science Paper 287, Colorado State University, Fort Collins, CO, 198 pp.
- Rocken, C., Y.-H. Kuo, W. S. Schreiner, D. Hunt, S. Sokolovskiy, and C. McCormick, 2000: COSMIC system description. *Terr. Atmos. Oceanic Sci.*, **11**, 21–52.

- Rotunno, R., and R. Ferretti, 2001: Mechanisms of intense alpine rainfall. *J. Atmos. Sci.*, **58**, 1732–1749.
- Schluessel, P., and W. J. Emery, 1990: Atmospheric water vapour over oceans from SSM/I measurements. *Int. J. Remote Sens.*, **11**, 753–766.
- Seitter, K. L., and H. S. Muench, 1985: Observation of a cold front with rope cloud. *Mon. Wea. Rev.*, **113**, 840–848.
- Smith, R. B., 1979: The influence of mountains on the atmosphere. *Advances in Geophysics*, Vol. 21, Academic Press, 87–230.
- Sokolovskiy, S., Y.-H. Kuo, C. Rocken, W. S. Schreiner, D. Hunt, and R. A. Anthes, 2006: Monitoring the atmospheric boundary layer by GPS radio occultation signals recorded in the open-loop mode. *Geophys. Res. Lett.*, **33**, L12813, doi:10.1029/2006GL025955.
- Stewart, R. E., J. D. Marwitz, J. C. Pace, and R. E. Carbone, 1984: Characteristics through the melting layer of stratiform clouds. *J. Atmos. Sci.*, **41**, 3227–3237.
- Stoelinga, M. T., and Coauthors, 2003: Improvement of microphysical parameterization through observational verification experiment. *Bull. Amer. Meteor. Soc.*, **84**, 1807–1826.
- Stohl, A., C. Forster, and H. Sodemann, 2008: Remote sources of water vapor forming precipitation on the Norwegian west coast at 60°N—A tale of hurricanes and an atmospheric river. *J. Geophys. Res.*, **113**, D05102, doi:10.1029/2007JD009006.
- Tapley, B. D., S. Bettadpur, M. Watkins, and C. Reigber, 2004: The Gravity Recovery And Climate Experiment (GRACE): Mission overview and early results. *Geophys. Res. Lett.*, **31**, L09607, doi:10.1029/2004GL019920.
- Wentz, F. J., 1995: The intercomparison of 53 SSM/I water vapor algorithms. Remote Sensing Systems Tech. Rep. on WetNet Water Vapor Intercomparison Project (VIP), Remote Sensing Systems, Santa Rosa, CA, 19 pp.
- White, A. B., D. J. Gottas, E. Strem, F. M. Ralph, and P. J. Neiman, 2002: An automated brightband height detection algorithm for use with Doppler radar spectral moments. *J. Atmos. Oceanic Technol.*, **19**, 687–697.
- Wick, G. A., Y.-H. Kuo, F. M. Ralph, T.-K. Wee, P. J. Neiman, and Z. Ma, 2008: Intercomparison of integrated water vapor retrievals from SSM/I and COSMIC. *Geophys. Res. Lett.*, in press.
- Wickert, J., and Coauthors, 2001: Atmosphere sounding by GPS radio occultation: First results from CHAMP. *Geophys. Res. Lett.*, **28**, 3263–3266.
- Zhu, Y., and R. E. Newell, 1998: A proposed algorithm for moisture fluxes from atmospheric rivers. *Mon. Wea. Rev.*, **126**, 725–735.